Rapid Optical Ptychographic Prototyping with Broad Bandwidth Illumination

by

(Jonathan) Tyler Reichanadter
BS Engineering Physics
BS Applied Mathematics

March 18, 2016

A Senior Thesis Submitted for Honors in Physics.
College of Arts & Sciences,
University of Colorado at Boulder May 2016

Co-Advisors

Henry Kapteyn Physics
Margaret Murnane Physics

Committee

Jamie Nagle Physics
Anne Dougherty Applied Math

Contents

1 Introduction

High-resolution microscopy is an important field of research that enables the study of physical, chemical, and biological phenomena. An immediate need for high-resolution microscopy can be found in the semiconducting industry. Each year, the features on integrated circuits are getting smaller and smaller. The ability to study the nano-scale structures on these circuits is critical for continued innovation. One pathway towards higher resolution microscopy is to use shorter wavelengths of light such as Extreme Ultraviolet (EUV) or x-rays. However, there is a lack of optics in this short wavelength regime since a majority of materials have a near-unity index of refraction and are strongly absorbing. This lack of optics presents an obstacle for traditional microscopy techniques based on lenses.

Our work explores the lensless imaging technique called Coherent Diffractive Imaging (CDI).[1–3] CDI works by illuminating an object with a highly coherent beam and measuring the diffraction pattern from the object with a detector. Using this data along with experimental constraints one can iteratively retrieve the phase of the diffraction and reconstruct the illuminated object (discussed in the Principle of Diffraction section of the Background).[4]

CDI presents several advantages to alternative microscopy techniques in the EUV spectrum. One, CDI is a lensless technique that is not limited by the fabrication quality of any optics. Second, CDI recovers a full characterization of how light interacts with the sample, offering both topographical and material information of the object. And third, CDI is a non-contact, non-destructive, method with a long working distance (centimeters).

This project's focus is to construct an optical CDI microscope for rapid prototype development of techniques and algorithms for multicolor experiments. CDI is often accomplished using a monochromatic beam, but in this experiment the probe will be polychromatic.[5] This multicolor illumination ptychography offers probe and object characterization for each color, meaning that ptychography identifies the spectral response of the object.[6] In this project I will explore multicolor ptychography using a broad bandwidth illumination (discussed in the Background).

This optical prototype will demonstrate the potential of hyperspectral ptychography in the EUV and x-ray spectral regions because CDI is not wavelength dependent. This is especially pertinent to tabletop sources generated by High Harmonic Generation (HHG, discussed in the Background).[7] Source produced by HHG is filtered for a single color, but now we can efficiently use the entire spectrum of the source and accomplish hyperspectral ptychography. The freedom to tune HHG wavelengths allows for elemental specificity when the wavelengths are resonant with absorption edges. Especially important are the carbon, oxygen and nitrogen edges that can be used study biological structures inside cells. Identifying the chemical specificity of a reconstructed image could have enormous application in the semiconductor industry for identifying defects within buried layers. The combination of short wavelengths, material contrast, and topographical information in a non-destructive microscope will be a valuable tool to explore problems across many fields.

2 Background

Ptychographic CDI is an advanced and powerful technique for imaging with resolution limited only by the wavelength and numerical aperture.[8] While the apparatus is minimal due to the absence of the image forming lens, the microscopy technique invokes sophisticated principles as it incorporates a multitude of various optical and mathematical ideas in order to capture an image. First CDI utilizes the principles of light diffraction and the Fraunhofer approximation[9] to form a propagator between the sample and the detector. Proper sampling of the diffraction must be considered when collecting the diffraction from the sample. Furthermore application of the Fraunhofer approximation requires the development of a computational method for recovering images. With ptychography the imaging process is modified for a scanning technique in which the sample is translated in the plane normal to the beam. At each scan position a diffraction pattern is collected and then is input into a ptychographic algorithm that reconstructs the fully scanned sample. Finally with recent investigation into hyperspectral microscopy it is necessary to understand the production of multi-color mode sources.

2.1 Principle of Diffraction

CDI is unique from traditional light microscopy in that no imaging forming optics are placed between the sample the detector. Instead, there is only free space propagation of the light diffracted by the sample. The diffracted light can be analyzed by considering Maxwell's wave equation.

$$\nabla^2 \vec{E} = \frac{1}{c^2} \frac{\partial^2 \vec{E}}{\partial t^2}$$

In general any function of the form $\vec{E}(x,t) = \vec{E}(x-ct)$ mathematically satisfies the differential equation (this is simplifying to one dimension). A more useful and physical solution to the Partial Differential Equation (PDE) is of the form $\vec{E}(\vec{r},t) = \vec{E_0}\ e^{i(\vec{r}\cdot\vec{k}-\omega t)}$, which is referred to as a planar wave. This wave is a simple monochromatic beam traveling in direction $\vec{k}$ with an amplitude and field direction given by $\vec{E_0}$. Note that the frequency and wavelength of this wave are $f = \frac{\omega}{2\pi}$ and $\lambda = \frac{2\pi}{|\vec{k}|}$ respectively. Not all waves are monochromatic (and consequently not always a continuous beam). Fortunately, electromagnetic waves superimpose linearly (and planar waves form a complete basis of integrable functions) so any other electromagnetic wave may be represented by a linear combination of monochromatic plane waves using Fourier decomposition. Such linear combinations describe the temporal profile of the wave. Thus there exists a reciprocal Fourier relation between time t and frequency k. This relation becomes important in ptychography for achieving high temporal resolution.

Characterizing Waves

Using knowledge of electromagnetic waves and their governing equation, the next step is to understand more on how a traveling wave propagates. Consider a monochromatic beam traveling in the $\hat{z}$ direction such that $\vec{k} = \frac{c}{\omega}\hat{z}$. Let this wave point in the $\pm\hat{y}$ so that we may revert to scalar notation. In studying propagation it is crucial to consider the spatial characteristic of the beam in the transverse plane. This beam may be characterized at a point in its trajectory (some $z = z_0$ along the propagation axis) by it's phase and amplitude $E = A\ e^{i\varphi}$ at each point in x-y. The value of A is the magnitude of the wave at the coordinate and φ is the phase (or relative time-delay) of the wave at the coordinate. Figure 1 shows the magnitude and phase of two different waves used in the prototype.

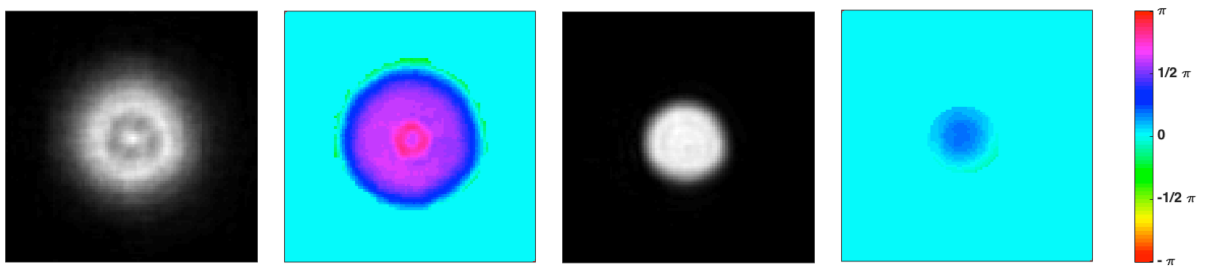

(a) Modulus, 450nm beam (b) Phase, 450nm beam (c) Modulus, 656nm beam (d) Phase, 656nm beam (e)

Figure 1: Lateral profile of experiment probes. Panels (a) and (b) show the amplitude and phase profile respectively of a blue probe with a wavelength of λ =450nm. Similarly panels (c) and (d) describe the amplitude and phase respectively for a red probe with λ =657nm. Grids for (a) and (b) are 173μm in length and grids for (c) and (d) are 252μm.

The gray-scale plots show the amplitude profile A of the beams, while the colored plots show the phase profile φ of the beams. The red probe in panels (c) and (d) has a relatively flat phase, varying by less than $\frac{\pi}{2}$ across the probe. Once knowledge of the amplitude and phase of the beam are known at a point along the beam's path, Maxwell's equations allow us to accurately predict the profile at other locations along the trajectory.

Fraunhofer Equation

An exit wave from the sample plane may be propagated using the PDE via numerical techniques such as the discrete time-step method and the spectral method (as conducted in the simulations section), yet these techniques can be computationally exhaustive. Fortunately there is a significantly quicker technique for shifting between the wave at the source and the diffraction provided a far-field assumption. The far-field assumption is that the transverse distance from the sample to the diffraction z satisfies the equation $z >> \frac{k}{2}\left(x^2+y^2\right)$ where k is the wave number and x, y are the lateral coordinates in the sample space. One of the most phenomenal results of Fourier optics is the Fraunhofer far-field diffraction equation.

$$f(u,v,z) = \frac{1}{\lambda z} e^{i\varphi} \int_{-\infty}^{\infty}\int_{-\infty}^{\infty} f_0(x,y)\ \ e^{-i2\pi\left(x\frac{u}{\lambda z}\ +\ y\frac{v}{\lambda z}\right)}\, dxdy$$

Figure 2: Visualization of the Fraunhofer diffraction equation. The plane with a green profile is the sample space where the probe illuminates the sample. The plane with a blue profile is the diffraction space which is necessarily far from the sample plane satisfying the far-field limit $z >> \frac{k}{2}\left(x^2+y^2\right)$.

As illustrated in Figure 2 the source wave is the initial function $f_0(x,y)$, where x and y are the coordinates in the plane at $z=0$. Additionally u and v are the coordinates in the diffraction plane, z is the distance of propagation from the source, λ is the wavelength of light, $\varphi = \frac{\pi}{\lambda z}\left(x^2+y^2\right) - \frac{\pi}{2}$ is the phase addition to the diffraction, and $f(u,v,z)$ is the diffraction. The detector cannot not directly measure the phase φ as the CCD camera cannot resolve phase information for IR, visible, or UV light.

Fourier Properties

The primary result of the Fraunhofer equation is:

$$f(u, v, z) \propto \ \mathcal{F}[\ f_0(x, y)\ ]$$

In this far-field regime the diffraction is proportional to the Fourier transform of the wave at the source. Rather than manually propagating the wave out to the plane of diffraction, the Fraunhofer equation provides an immediate computation for switching between the source and diffraction. Although the Fraunhofer equation is valid in the far-field region, it still holds valid between the exit wave of a convex lens and the focal distance from the lens.

The Fraunhofer equation describes a relation between the source and diffraction that allows for a more computationally efficient propagation of the wave. Additionally it provides a framework for understanding the relationship between the two spaces. For instance a larger range of spatial frequencies in the diffraction space correspond to more finely resolved images in the sample space.

Another key consequence of the Fraunhofer equation is the principle of scaling. Fourier transforms carry a reciprocal relationship between their base coordinates and their transform coordinates. In this situation the base coordinates are the sample's spatial coordinates x,y, which suggests that the transform coordinates are spatial frequencies k_x and k_y. Physically the diffraction is not presented in spatial frequencies, and this discrepancy is qualified by the scaling constant λz in the fashion $k_x = \frac{u}{\lambda z}$ and $k_y = \frac{v}{\lambda z}$. This constant bridges the two spaces and is prominent in resolution and oversampling calculations, which will be explained later in the Background.

2.2 Resolution and Sampling

Lensless imaging techniques can achieve a spatial resolution bounded only by the theoretical limit. As opposed to alternative microscopy methods, CDI removes any resolution loss due to the fabrication quality of lenses and extends conveniently into the EUV and X-ray region of the electromagnetic spectrum. The latter advantage is particularly key as increasing the frequency of the illumination pushes microscopy into a higher-resolution regime. The theoretical lateral resolution is given by Abbe's resolution limit $R = \frac{\lambda}{2N_a}$, in which R is the smallest separation capable of being resolved.[10] Since the objective is to minimize R, it becomes essential to minimize λ and maximize N_a. The numerical aperture N_a is determined by the microscope's geometry.

Figure 3 illustrates the transmitted diffraction from a small slit (which will later be substituted by the sample) onto a flat surface. The numerical aperture is the *sine* of the measured diffraction angle multiplied with the index of refraction. The transmitted wave from the slit propagates in all directions so an ideal detector would extend out infinitely and measure $sine(\theta = 90^{\text{o}}) = 1$, however cameras may only measure a finite area so the *sine* is restricted between $(0, 1)$.

The index of refraction is approximately unity as the medium of propagation is either air or vacuum. This suggests the optimal resolution is $R = \frac{\lambda}{2}$. The detector has a CCD chip length of 5mm and the propagation distance is 20mm, which admits a numerical aperture of $N_a = 0.13$ and resolution of approximately $R = 4\lambda$.

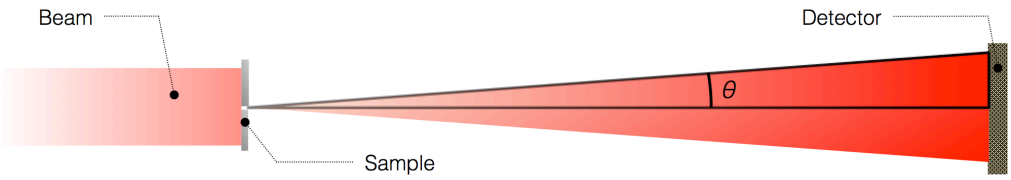

Figure 3: Numerical Aperture is given by the equation $N_a = n\ Sin(\theta)$. This aperture plays a direct role in the theoretical maximal resolution capable for the CDI microscope. A larger numerical aperture provides a finer spatial resolution. The index of refraction n for air is $n = 1.00029$.

Another crucial element to consider about the detector is its discretization of the diffraction. Pixels have finite size and store the transmitted diffraction by pixels spaced finitely apart. This digital storage does not directly impact the resolution though. Rather than the pixel size corresponding to the spatial coordinates of the sample, the pixel size corresponds to the spatial frequencies of the sample. A pertinent consequence of the Fourier transform relationship between the sample and the detector is the *Fourier Uncertainty Relation*. This relation provides a unit conversion between the sample-space and the diffraction space

$$du\ dx = \frac{\lambda\ z}{S}$$

In this relation u is the coordinate in the diffraction space and x is the coordinate in the sample space. The variable S is the number of pixels across the detector. This transformation is homeomorphic, meaning that $S \times S$ pixels in the diffraction space correspond to $S \times S$ pixels in the sample space.

The finer (smaller) each pixel du is on the CCD, the larger each pixel in the recovered sample dx. This naturally leads to the concern of whether the pixel lengths du are sufficient in order to capture the full sample in the image (see Figure 4). It can be assured that the image is properly sampled by satisfying what is called the *over-sampling* condition.[11] Oversampling is a dimensionless value that indicates whether there is sufficient frequency data to reconstruct the image. This is equivalent to Nyquist sampling the intensity of the diffraction pattern. An equation for oversampling is provided below.

$$\boxed{O_S = \frac{\lambda\ z}{p\ W} \geq 2}$$

The numerator $\lambda\ z$ is the scaling factor found for Fraunhofer diffraction, p is the length of the detector pixels (equivalent to du), and W is the largest diameter of the exit wave. As might be expected, if the exact analog diffraction could be stored (so $p \to 0$) then the oversampling condition would be always be satisfied.

The figure below shows the immediate consequence of under-sampling. If the oversampling condition is not met, then by the Fourier uncertainty relation the sample grid will not contain the image. In Figure 4 the left image shows an exit wave of a frog that extends nearly to the ends of the imaging grid, meaning that the corresponding diffraction is near the sampling limit ($O_s \approx 2.1$).

After binning the diffraction by 4 the image is under-sampled ($O_s \approx 0.5$) and the resulting exit wave no longer fits within the grid. Additionally the cropped regions of the frog reappear as artifacts on the resulting wave. An equivalent understanding of over-sampling may follow from considering the sampling of simple sine waves in one dimension. Imagine that there are two sine waves with a 2:1 frequency ratio between them. In the frequency space these would simply be two unique points.

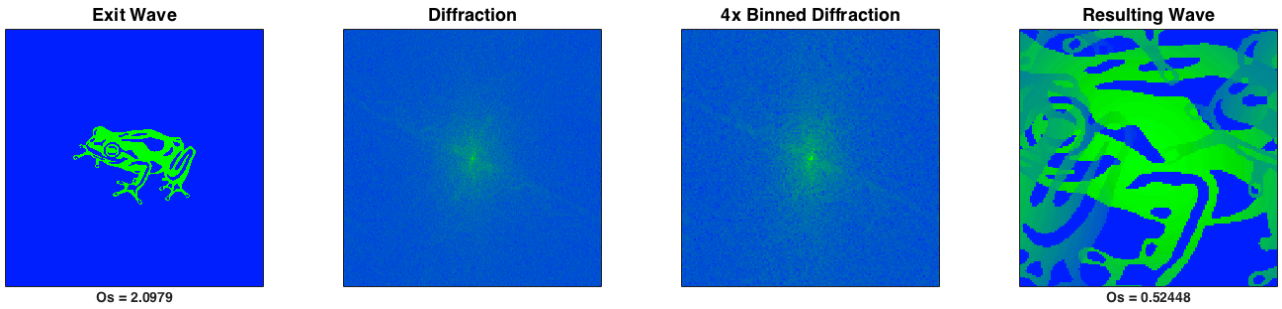

Figure 4: Consequence of under-sampling. The initial exit wave is sufficiently sampled so that the object inhabits roughly one fourth of the spatial region. After binning the diffraction by four the reconstruction is undersampled.

(a) Two unique spatial frequencies.

(b) Consequence of undersampling sine waves.

Figure 5: Two sine waves illustrating an undersampling condition in which the two waves are indistinguishable.

If the camera's pixels were too large they might not read all of the frequencies correctly. Imagine that these sine waves are equivalent to the points $k = 0.5$ and $k = 1$ in the Fourier transform space, yet the k-space is sampled by integers. The result is illustrated in panel (b) of Figure 5.

The higher frequency is misinterpreted as equivalent to the lower one. The green points represent the sampling and the overlap of the functions at these points indicates that these functions appear identical. The misinterpretation of frequency data leads to the overlapping artifact in the resulting exit wave.

2.3 Iterative Methods for Phase Retrieval

The key challenge facing CDI is recovering the object from the modulus of its diffraction. Unfortunately a CCD detector cannot attain any information about the phase of the light incident upon the camera, which essential for propagating the diffraction back to the sample. This challenge is mathematically postulated by representing the known data by

$$I(u,v) = \left| \int\int f(x,y)\ e^{2\pi i(xu+yv)}\ dxdy \right|^2$$

and proposing to find the solution to $\varphi(u,v)$ from

$$F(u,v) = \sqrt{I(u,v)}\ e^{i\varphi(u,v)}$$

The challenge had been first solved using a modified form of the Gerchburg-Saxton algorithm from electron microscopy.[12] Since then various modifications have been made to the original algorithm, yet the core stages have persisted. It begins by initializing a phase guess $\varphi_1(u,v)$ for the diffraction. The first guess of the full diffraction is $G'_1(u,v) = \sqrt{I(u,v)}e^{\varphi_1(u,v)}$. The algorithm then iterates (for $k \in \mathbb{N}$) as follows.

First Take the inverse Fourier transform $g'_k = \mathcal{F}^{-1}[\ G'_k\ ]$

Second Apply domain constraint (varies based on algorithm) $g_{k+1} = f(g'_k)$

Third Forward transform the new solution guess $G_{k+1} = \mathcal{F}[\ g_{k+1}\ ]$

Fourth Apply the diffraction constraint $G'_{k+1} = |G_{k+1}|\ e^{\varphi_{k+1}} \quad \rightarrow \quad G'_{k+1} = \sqrt{I}\ e^{\varphi_{k+1}}$

After applying the diffraction constraint this algorithm repeats and converges to the correct phase φ and thus to the solution g. Figure 6 below illustrates an intuitive understanding of the algorithm. First a random guess of the phase of the diffraction is taken (start) in the space of square integrable functions $\mathcal{L}^2$. Next the phase is paired with the measured diffraction (represented by the curve connecting the start point to the blue modulus constraint space) and propagated back into the sample space (the following curve to the green domain constraint space).

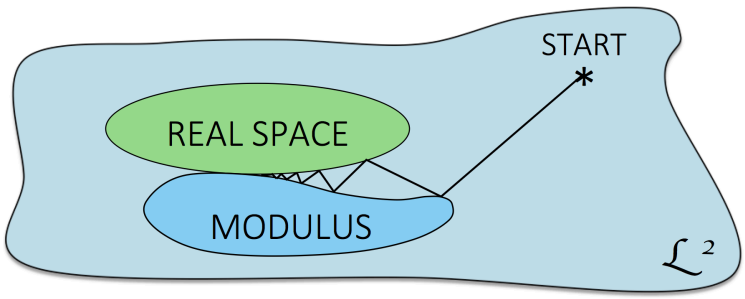

Figure 6: Visual representation of the iterative reconstruction algorithm

Then a filtering is applied to the guessed object that makes it a better guess and the adjusted picture is forward propagated into the diffraction space (via the Fourier transform). Finally the corresponding diffraction guess is adjusted to have the same modulus as the measured diffraction (shown by the curve that follows from the green domain space back to the blue modulus space) and the algorithm is repeated.

One thing that is rather important is that the collected diffraction pattern is in the far-field limit so that the Fraunhofer approximation is valid. This algorithm is based on the propagator for the sample wave being a Fourier transform. If this were not the case, then the algorithm would require a new computational method for traveling between the sample and diffraction spaces.

For the domain constraint there exist a variety of possible functions that may be applied. For example, if the approximate area in which the sample resides is known, then it may be sufficient to zero pad outside of the support for the domain constraint. In fact this is a powerful constraint that is practically necessary for convergence to a correct solution. So if γ represents the space in which the sample resides, then the domain constrain would appear as

$$g_{k+1} = f(g'_k) = \begin{cases} g'_k & \in \gamma \\ 0 & \text{else} \end{cases}$$

This region γ is called the support, and in order for the algorithm to converge towards the correct object it is imperative to have a support that limits the object to under half of the total spatial domain. Fortunately the oversampling condition guarantees this will be satisfied. The algorithm fails from an insufficient support γ because there would otherwise be too many possible solutions to the provided constraints. Visually one can imagine an insufficient γ by growing the *Real Space* region from Figure 6 so that it overlaps with the *Modulus* region. This suggests there is a family of solutions, where in fact there is only one physical solution.

One modification of the error reduction algorithm is the input-output method (equations are adapted from this reference).[13] This method was developed to increase the rate of convergence to the solution by utilizing a negative feedback technique which attempts to compensate for the imposed modulus constraint on the next iteration. The input-output algorithm modifies the domain constraint to

$$g_{k+1} = f(g'_k) = \begin{cases} g_k & \in \gamma \\ g_k - \beta g'_k & \text{else} \end{cases}$$

in which β is the feedback parameter within 0 to 1. The object guess g_k indicates the guess after satisfying the domain constraint from the previous iteration. Another modification to the reconstruction algorithm is the Hybrid Input-Output (HIO) method. HIO applies an alteration to the domain constraint by combining elements from both error reduction and input-output method. Specifically the domain constraint matches the error reduction method within the support and matches the input-output method outside of the support

$$g_{k+1} = f(g'_k) = \begin{cases} g'_k & \in \gamma \\ g_k - \beta g'_k & \text{else} \end{cases}$$

All three modifications of the image reconstruction algorithm share identical form with the exception of the domain constraint function. Even for a sufficient support γ these algorithms may have either multiple solutions or no solution at all. In the event there is no solution the algorithm determines the *best guess* which minimizes the distance to a correct solution with respect to the error metric

$$E_k = \frac{\sum(\ |G_k(u,v)| - \sqrt{I(u,v)}\ )^2}{\sum I(u,v)}$$

where the sum spans over all of the coordinates in u,v space. Evidently if the final object guess has the correct diffraction modulus then $|G_k(u,v)|^2 = I(u,v)$ and as a result $E_k = 0$. The alternative is multiple solutions in which there are various objects that satisfy the modulus constraint. With most choices of support γ this is ultimately the case.

The Fourier transform modulus is blind to object translations and flips. Without a support γ that specifies the rotation and position of the object precisely there are multiple solutions to the phase retrieval problem. This becomes an issue when the algorithm changes which orientation of the object to converge to between interactions. One way to reduce the challenges associated with the flip and position ambiguities includes implementing a dynamic support γ_k. As the algorithm iteratively guesses at the object, the support within the algorithm changes by wrapping about positive regions in the sample. Routinely the support γ_k reduces its number of points in u,v space, thus modifying the domain constraint to favor a particular orientation of the object. This modification to the domain constraint is called *shrink wrapping*. Figure 7 illustrates the results I achieved from implementing shrink wrapping to the HIO algorithm.

Image reconstruction algorithms are capable of converging to the object provided a diffraction pattern and an object domain constraint. These algorithms restrict the object through the domain support constraint and the oversampling condition. Ptychography relaxes these isolation restrictions on the sample, yet still utilizes this phase retrieval technique.

2.4 Ptychography

Ptychography is a CDI technique in which the probe translates across the object in the transverse plane and a diffraction pattern is collected at each translated position.[14] The translations are necessarily less than the width of the probe, meaning that the collected diffraction patterns contain overlapping sample information. This redundancy in information provides the added advantages of not requiring a finite object support. Additionally the ptychographic algorithm solves for more than the exit wave from the sample. Ptychography is capable of distinguishing the object from the probe illuminating the object, rather than single-diffraction CDI that is only capable of reconstructing the exit wave from the sample. In ptychography it is necessary to make this distinction as a single probe illuminates different portions of the sample.

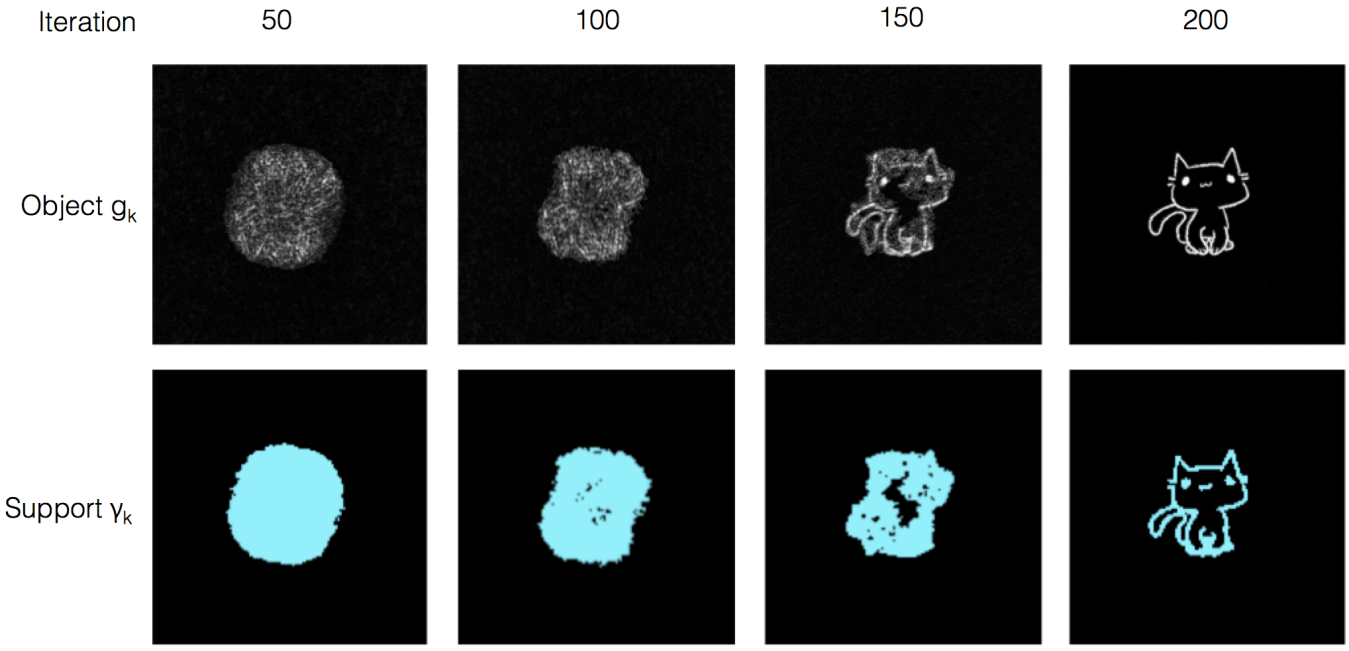

Figure 7: Operation of the HIO image reconstruction implementing shrink wrapping. Every ten iterations of the algorithm the support γ_k is adapted to enclose the most recent object guess g_k. Shrink wrapping is an advantageous modification as it forces the algorithm to favor a particular object orientation and remove the flip/position ambiguities associated with the Fourier transform.

In Figure 8 multiple exit waves from a ptychographic scan simulation I created reveal the relationship between the object and the probe. A single circular probe travels in a 3×3 grid about a central point of the sample. At each scan position there is a unique exit wave (white) created with the probe and some sub-region of the object.

Figure 8: Cascading images of the exit wave amplitudes from a 3×3 scan grid. These images show the exit waves from a ptychography simulation. The dark gray regions indicate the non-illuminated object, the light gray regions indicate the illuminated area where the object is opaque, and the white regions indicate the actual exit wave.

For visual purposes Figure 8 reveals the object, the probe, and the exit wave together while only the exit wave itself is diffracted onto the CCD camera. The diffraction from each of these exit waves is shown in Figure 9.

Each single diffraction pattern can be input into a phase retrieval algorithm such as error reduction method or HIO method to retrieve the exit wave. However, together the diffractions may be input into the ptychographic algorithm from which both the probe and object can be discerned.

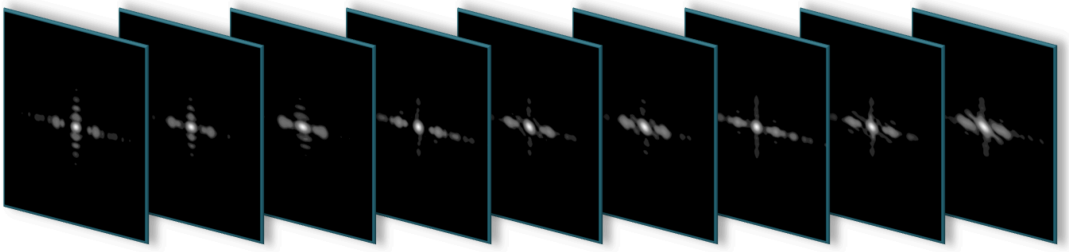

Figure 9: Diffractions from the 3 x 3 scan grid shown in Figure 8. The image shows the diffraction pattern from a scan position in a ptychography simulation. Each image is the modulus of the Fourier transform for the corresponding exit wave (white regions from Figure 8)

Although ptychography implements similar iterative methods used for the single-diffraction problem for phase recovery, the extension to multiple scans at various sample positions demands additional notation. There are four different indices used throughout ptychography (including a color index for hyper-spectral ptychography); these indices are for algorithm iterations k, scan position j, color λ, and pixel index $\mathbf{x}$.

$$\mathbf{x} \in [1, X_{max}] \oplus [1, Y_{max}] = X \qquad \begin{array}{l} X_{max} = \text{number of CCD pixels across} \\ Y_{max} = \text{number of CCD pixels down} \end{array}$$

$$k \in 1, 2, ..., It_{max} = K \qquad It_{max} = \text{total number of algorithm iterations}$$

$$j \in 1, 2, ..., J_{max} = J \qquad J_{max} = \text{number of scans collected}$$

$$\lambda \in 1, 2, ..., C_{max} = \Lambda \qquad C_{max} = \text{number of frequencies}$$

Previously the object guess for a given iteration was noted by a lower case g, where now the analogous exit wave is noted by ψ and the Fourier transform of the exit wave is respectively noted by Ψ. As considered above the assumption on the exit wave is that the wave is a product of the sub-object and the probe. For ptychography (single color mode) the equation for the exit wave (at each position) is $\psi_{k,j}(\mathbf{u}) = P(\mathbf{x} - \mathbf{r}_j)\ O(\mathbf{x})$ in which the function $P(\mathbf{x} - \mathbf{r}_j)$ is the probe (translated to match the scan position using the scan position vector $\mathbf{r}_j$) and $O(\mathbf{x})$ is the object. In hyperspectral ptychography an exit wave is discerned for each wavelength[15] and so the reconstruction algorithm implements a more evolved equation (equations are adapted from[14]) .

$$\psi_{k,j,\lambda}(\mathbf{x}) = \sqrt{\frac{S_{k-1,j,\lambda}}{\sum_{\mathrm{x}\in X} |P_{k,j,\lambda}(\mathbf{x})|^2}}\ P_{k,j,\lambda}(\mathbf{x})\ O_{k,j,\lambda}(\mathbf{x}) \tag{1}$$

The function $S_{k,j,\lambda}$ is the spectral weight function of the probe. When normalized by its sum, the spectral weight function provides a spectral profile of the probe. Notice that the spectral weight function is dependent on the scan position, so to attain relative spectral weights from the function it is necessary to average over the scan positions. The function for the spectral weight function is provided by

$$S_{k,j,\lambda} = \sum_{\mathrm{x}\in X} |P_{k,j,\lambda}(\mathbf{x})|^2$$

It is evident that once the spectral weight function converges ($S_{k-1,j,\lambda} = S_{k,j,\lambda}$) then the square rooted expression in Equation 1 becomes unity and the simple product relation of the exit wave is preserved. Once the exit wave is established the wave may be forward propagated to the diffraction space, which under the Fraunhofer far-field assumption relates the two spaces by the Fourier transform.

$$\Psi_{k,j,\lambda}(\mathbf{u}) = \mathcal{F}[\ \psi_{k,j,\lambda}(\mathbf{x})\ ] \tag{2}$$

While x indicates the sample space coordinate and u indicates the diffraction space coordinate, both variables span an $S \times S$ grid as explained in the Background $\mathbf{x}, \mathbf{u} \in X$. The propagation is implemented on each exit wave, that is, for each scan position j and color λ. Just as with the single-diffraction iterative methods the modulus constraint is implemented to the transformed exit waves.

$$\Psi'_{k,j,\lambda}(\mathbf{u}) \;=\; \sqrt{\frac{I_j(\mathbf{u})}{\sum\limits_{\lambda\in\Lambda} |\Psi_{k,j,\lambda}(\mathbf{u})|^2}}\;\; \Psi_{k,j,\lambda}(\mathbf{u}) \tag{3}$$

$I_j(\mathbf{u})$ represents the measured diffraction intensities at each scan position. The predicted diffraction pattern is modified to satisfy the modulus constraint at each position. This equation assumes the coherence of the multiple color modes composing the probe. Next the diffraction is propagated back to the sample space using the Fourier propagator.

$$\psi'_{k,j,\lambda}(\mathbf{x}) \;=\; \mathcal{F}^{-1}[\; \Psi'_{k,j,\lambda}(\mathbf{u}) \;] \tag{4}$$

After the modified exit wave is attained by restricting the wave to satisfy the diffraction modulus constraint, the only stage remaining is to update the object and probe using the modified exit wave. In the single-diffraction iterative algorithms the updates are defined using the support γ combined with the specific method's function. In ptychography the update function is of a different form that does not apply any support (other than the scanning overlap condition).

$$O_{k+1,j,\lambda}(\mathbf{u}) \;=\; O_{k,j,\lambda}(\mathbf{x}) \;+\; \alpha\; \frac{P^*_{k,j,\lambda}(\mathbf{u})}{|P_{k,j,\lambda}(\mathbf{u})|^2_{max}} \left(\psi'_{k,j,\lambda}(\mathbf{x}) - \psi_{k,j,\lambda}(\mathbf{x})\right) \tag{5}$$

$$P_{k+1,j,\lambda}(\mathbf{u}) \;=\; P_{k,j,\lambda}(\mathbf{x}) \;+\; \beta\; \frac{O^*_{k,j,\lambda}(\mathbf{u})}{|O_{k,j,\lambda}(\mathbf{u})|^2_{max}} \left(\psi'_{k,j,\lambda}(\mathbf{x}) - \psi_{k,j,\lambda}(\mathbf{x})\right) \tag{6}$$

The parameters α and β influence the updated probe and object and are considered the step sizes with respect to the error metric. The object update Equation 5 effectively averages the new object with the previous object. It accomplishes this by attaining the objects from both the new and previous exit waves, and then using these to adjust the previous object. The probe update function works in a similar fashion.

These equations comprise the ePIE ptychography algorithm. Ultimately the form of the ptychography algorithm matches closely with the iterative methods discussed earlier. They key advantage now is that the domain constraint is removed by the overlapping property of the scans. Additionally this overlap admits sufficient data to distinguish the probe and object from the exit wave and determine the relative spectral weights of the probe.

2.5 Broad Bandwidth Source

Hyperspectral ptychography offers multiple key advantages over single color ptychography.[18,19] With object and probe reconstructions for each sampled wavelength, the recovered information can provide information on the spectral response of the sample as well as provide extended topographical information using the reconstructed object phases. Ptychography is popular in the EUV region of the electromagnetic spectrum for its superior resolution limit to visible light, which may be produced using HHG. HHG works by evoking a nonlinear interaction within a gas using high-intensity laser pulses.[20–22] A tuned driving laser of lower frequency is focused down into a wave guide where the beam excites atoms in a high-density gas with multiple photons per atom (producing the non-linear response). The ultraviolet emission from each electron-atom recombination adds constructively to generate bright extreme ultraviolet pulses.[23]

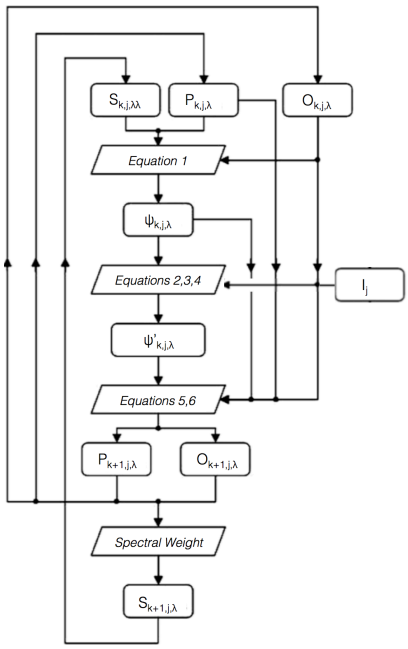

Figure 10: Figure adapted from[14] . Flowchart describing the ePIE algorithm for hyper-spectral ptychography. Initial guesses are made for the object, spectral weights, and the probe. Then those functions are input into the exit wave equation where then the exit wave is updated by the collected diffraction intensity. Finally new guesses for the object, spectral weights, and probe are made using the updated exit wave.

Figure 11 shows the emitted spectrum from HHG with a diffraction grating placed after the waveguide. The multiple colors on the plot after the grating indicate the spectrum produced from different driving laser wavelengths (yellow is 0.8μm, green is 3μm, blue is 2μm, and violet is 3.9μm). The result of HHG is a comb frequency distribution in the EUV region. This is a result of the quantized ionization states of the electrons within the gas.

These combs are the harmonic frequencies of high harmonic generation. Most ptychography experiments in the Kapteyn-Murnane group use HHG as a tabletop source for EUV light, yet they filter the illumination for a single harmonic. Not only is filtering a less efficient use of the generated source, but incorporating the full spectrum into the illumination extends the advantages of CDI via hyperspectral ptychography. Furthermore many fascinating samples (for instance, samples containing Oxygen, Water, Silicon, Carbon, or Nitrogen) have unique spectral responses in the EUV regime that could be detected using multiple frequencies within this portion of the spectrum.[24] The optical ptychography prototype will demonstrate the potential of utilizing multiple harmonics by utilizing a spectrum with a broadband source.[25]

The optical hyperspectral ptychography prototype will reconstruct the image of an object using a source with a broad bandwidth spectrum in the IR region. A perfect source for this broadband light is the seed laser used for HHG, which is a Ti:Sapphire oscillator with a maximum gain in the IR region. The oscillator is pumped using a high-intensity 532nm laser. Once mode locked the oscillator outputs the spectrum shown in Figure 12.

I measured the spectrum using an Ocean Optics 2000+ Spectrometer and saved the data in a *.txt* file that is convertible into Matlab. Successful reconstructions using this broad bandwidth source will serve as proof-of-concept for hyper-spectral ptychography using a HHG source.

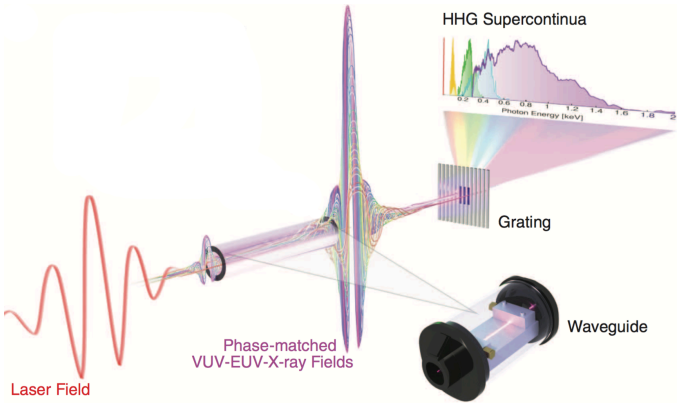

Figure 11: Figure adapted from.[25] High harmonic generation. A driving laser focuses down into a waveguide and creates a strong electric field that evokes a nonlinear response from the gas within the waveguide. The extreme laser field excites electrons from their parent atoms using multiple photons and the recombination emits discrete frequencies of light. By tuning the driving laser properly one can force the electromagnetic emission from the atoms to add constructively forming a coherent source.

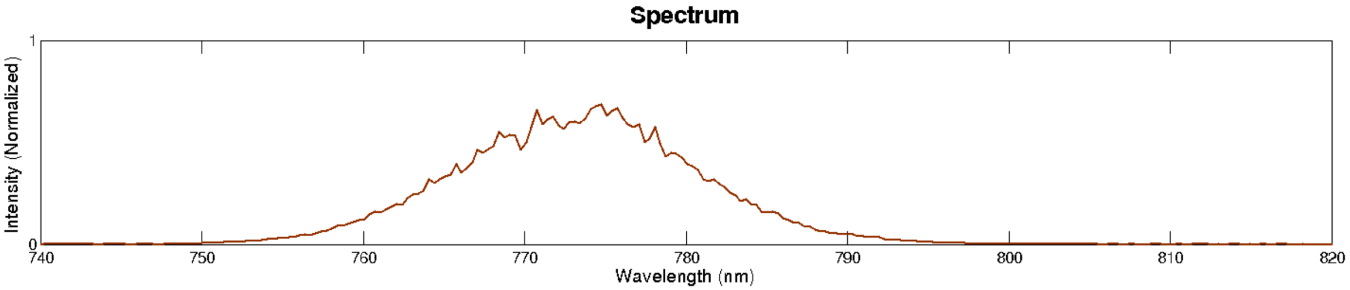

Figure 12: Output spectrum from the mode-locked Ti:Sapphire oscillator. Typically this source is used to seed an amplifier, which is then focused into a waveguide as a driving field for HHG. But for the prototype this source will be used directly as the illumination. Successful reconstructions using this broad bandwidth source will serve as proof-of-concept for hyperspectral ptychography using a HHG source.

3 Simulations

The ptychography prototype is a newly designed and implemented experimental apparatus. I needed to build the experiment starting from the ground up, first assembling the prototype for single-diffraction CDI, then progressing through the stages until the microscope could test the hyperspectral algorithm. At each major stage of the project it became useful to verify the expected results from experiment using Matlab simulation. In particular there were three useful simulations for this project.

The first simulation demonstrates the effectiveness of the iterative phase retrieval algorithm at reconstructing an image based on the intensity of its far-field diffraction pattern. In this simulation I test different modifications of the error reduction method to achieve a reconstructed image.

My second simulation scans an $n \times n$ grid using a circular probe on a simulated sample and then generates a collection of far-field diffraction patterns from the scan positions. This data can be input into the ptychographic algorithm to attain a reconstruction of the sample and the probe.

My third simulation implements the Helmholtz equation in order to propagate a probe along the optical axis. This simulation has particular application in debugging the experiment. In fact a reconstructed probe from ptychography may be input into the simulation and propagated to determine any misalignment in the system.

3.1 Simulated Phase Retrieval

The detector I have used for the prototype is a Mightex SS USB3.0 CMOS camera. This device has a minimum exposure time far exceeding the oscillation frequency of the exit wave, so the detector can only measure the intensity information of the diffraction. In order to recover the image from the diffraction pattern it is necessary to use one of the iterative algorithms discussed in the Background section. This simulation takes an exit wave, propagates it using the Fourier transform, and discards the phase of the propagated wave. With only a diffraction pattern amplitude and a support for the object, the simulation reconstructs the image. Figure 13 shows the initial information created in the simulation.

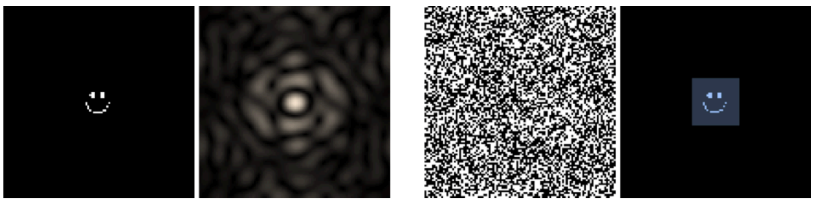

Figure 13: Starting information for single-diffraction phase retrieval simulation. (a) Exit wave being imaged. (b) Intensity of the exit wave. The diffraction is in the far field so it is the modulus of the 2D spatial Fourier transform of the exit wave. (c) Initial guess for the phase of the diffraction, completely random for this simulation. (d) The support γ overlaid with the exit wave to show that the sample resides within the support.

Notice that the support γ contains and isolates the sample to a smaller portion of the grid. Now the algorithm uses the intensity as a diffraction space constraint and the support γ as a sample space constraint to begin converging towards a solution. First the simulation is set to use the Error Reduction method, which crops the exit wave via the support.

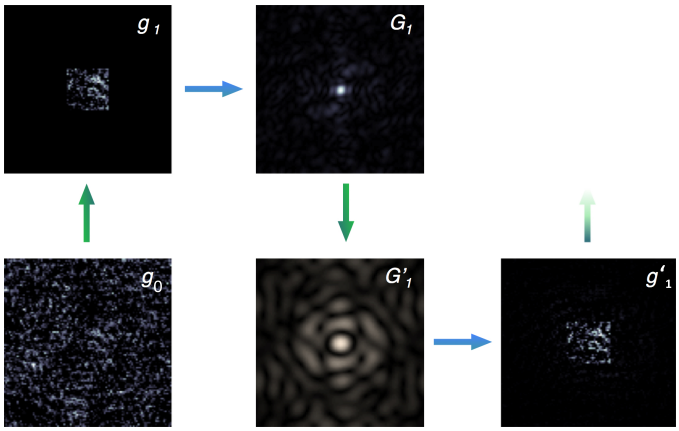

Figure 14: Illustration of the first steps in the Error Reduction algorithm (green arrows show constraints and blue arrows show propagation). First, the random phase paired with the modulus data is propagated to make the first guess (g_1, bottom left). Then, the guess is updated by cropping everything outside of the support (g'_1, top left). Next, this updated guess is propagated to the diffraction space (G_1, top center), and then this propagated guess replaces its amplitude with the diffraction constraint (G'_1, bottom center). After the diffraction constraint is applied this updated diffraction is propagated back into the sample space (g_2, bottom right) forming a new guess that repeats though the algorithm.

Figure 14 walks through the first few steps of the Error Reduction algorithm. First, the random phase is paired with the modulus data and propagated to the sample space making the first guess g_1 is in the bottom left of Figure 14. Then, the guess is updated by setting all values outside of the support to zero while leaving the region within the support unaffected (updated guess g'_1 is located in the top left). Next, this updated guess is propagated to the diffraction space via the Fourier transform to form G_1 in the top center of Figure 14. Afterwards, this propagated guess replaces it's amplitude with the diffraction

constraint created at the start of the simulation so that $|G_1'| = \sqrt{I}$ (shown on the bottom). Finally, the updated diffraction guess is propagated back into the sample space forming the next guess g_2 in the bottom right. Note that the guess has not yet been constrained to the support, so the algorithm has already made a significant jump towards the correct solution. After multiple iterations I attain the following results:

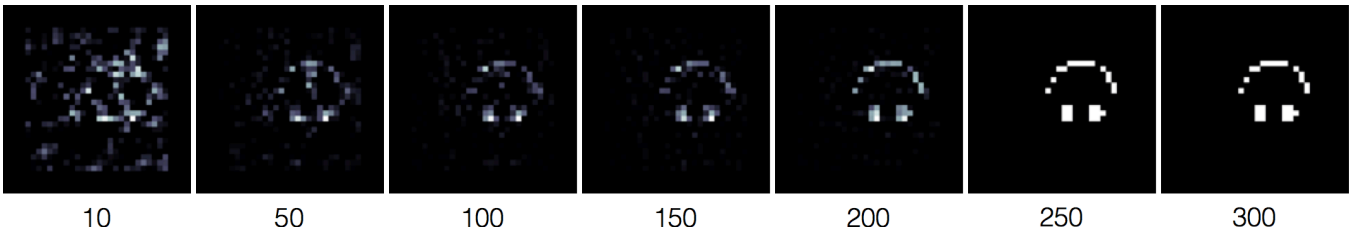

Figure 15: Exit wave guesses from the single-diffraction phase retrieval simulation. The numbers below each image indicate the iteration in the Error Reduction algorithm at which the guess was made. The guesses have been magnified for more convenient viewing. These results also illustrate the flip-translation ambiguity associated with single-diffraction CDI.

The algorithm successfully attains the exit wave from the diffraction modulus and the provided support. Notice that the smiley face is flipped vertically and shifted from the center. The flip and shift ambiguity is a consequence of the Fourier transform propagator on a single diffraction that vanishes when shifting towards ptychography. As covered in the Background the error metric for the iterative algorithm is the square difference between the guess's diffraction and the measured diffraction

$$E_k = \frac{\sum(\ |G_k(u,v)| - \sqrt{I(u,v)}\ )^2}{\sum I(u,v)}$$

For this simulation of the error reduction algorithm, the resulting error measurement at each iteration is shown in Figure 16 below

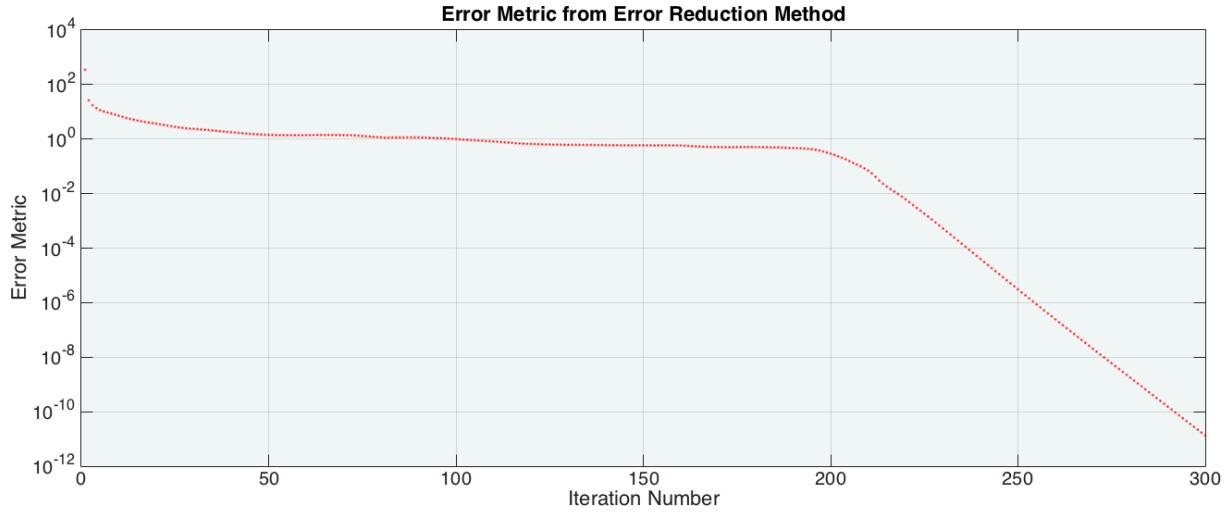

Figure 16: Measured relative error after each iteration of the error reduction algorithm shown on a semi-log plot.

As shown by the error metric and the final guess after 300 iterations, the error reduction algorithm can recover the phase of the diffraction pattern provided that the sample is sufficiently isolated.

3.2 Simulated Ptychography Scanning

For my second simulation I built a program that collects scanning data from a computer-generated sample. The code offers a great degree of freedom in terms of customizing the sample, probe, scanning overlap, and frequency of probe. Primarily this simulation demonstrates that the optical geometry of the prototype satisfies all of the necessary conditions in order to recover an image of the object and the probe. In order to model the experiment it is necessary for me to attribute physical units to the chosen elements of the simulation. The probe is chosen to be a flat, circular aperture with a diameter of 75 μm. Since I knew the model of the camera in the prototype, I used the pixel size provided on the detector's manual $5.2\mu m$, as the distance unit du in the diffraction space. Figure 17 shows a screenshot of the ptychography simulation collecting data by scanning the probe over the computer generated sample. The left image shows an image of the sample plane during data collection and the right image shows what the camera records at this scan position. The probe moves in an 11×11 grid collecting a diffraction at each position.

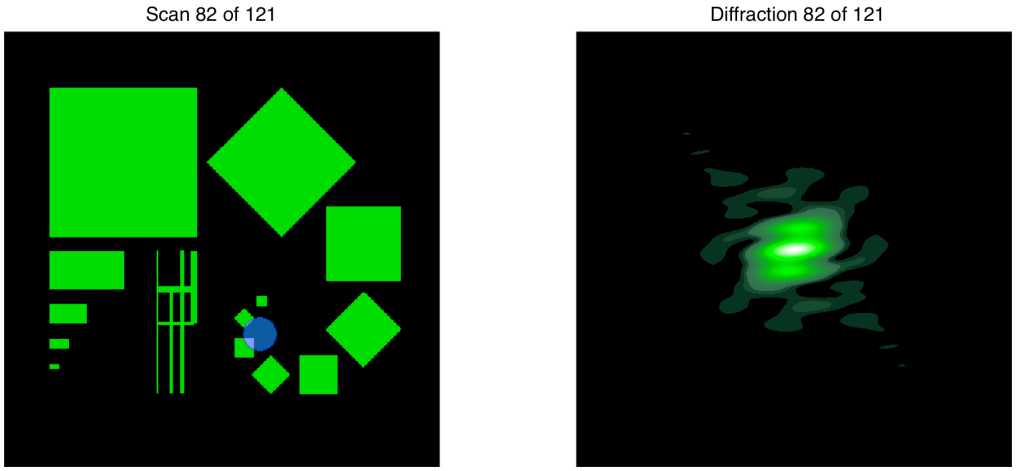

Figure 17: Screenshot of the ptychography simulation during data collection. On the left the object is illustrated by the green region while the probe scanning across the sample is shown by blue. This probe is $75\mu m$ in diameter and the sample stretches $2.5mm$ by $2.5mm$. On the right is the recorded diffraction on the detector from the exit wave illuminated by the probe (light blue on the left). The detector is $5.2mm$ by $5.2mm$.

This figure only reveals one scan of the 121 total scan positions. In order to attain the distance unit in the sample space it was necessary to specify the wavelength of the illumination, which was chosen to be the wavelength of the red laser diode for the prototype of 657nm, and specify the distance from the sample to the detector, which was 20mm. The simulated detector had a 1008×1008 pixel array, rendering the distance unit in the sample space of $2.5\mu m$.

This simulation does not scan the entire sample, but rather only records diffractions of a small section of the sample. Ptychography requires a large amount of overlap between scans; for this simulation the scans overlap 75% by area in an 11×11 grid. Furthermore the ptychographic algorithm prefers that the scan positions do not form a symmetric map, so in the simulation the scan positions have been given a random shift from expected position by up to 6% each. Figure 18 shows the scanned region in the simulation both with and without the probe positions outlined.

There is no isolation requirement on the object as Figure 18 illustrates that the scanned object has features along the edge of the scan grid. To test the capabilities of the ptychography algorithm at reconstructing both the object and the probe a false probe is fed into the program. This probe is not strictly constrained as with the known probe, but rather given by a Gaussian spatial profile that decays to $1/e$ after a diameter of $75\mu m$. For the first 30 iterations the probe is fixed as this Gaussian beam, then the algorithm updates the probe. The results are illustrated in Figure 19.

(a) Simulation scan including probe scans overlaid.

(b) Simulation scan (object). Grid is $225\mu m$ by $225\mu m$.

Figure 18: Resulting scanned region from the ptychography simulation ($225\mu m \times 225\mu m$ area) using a $75\mu m$ probe with 75% overlap and 6% randomness to the scan positions. Panel (a) overlays a gold outline of the probe at each scan position with a bolded outline to emphasize the probe shape on the sample. Panel (b) shows the scanned region where the white region is the transmitted exit wave, the black region is the scanned negative of the sample (light reflects off of the sample), and the burgundy region is the unscanned part of the sample.

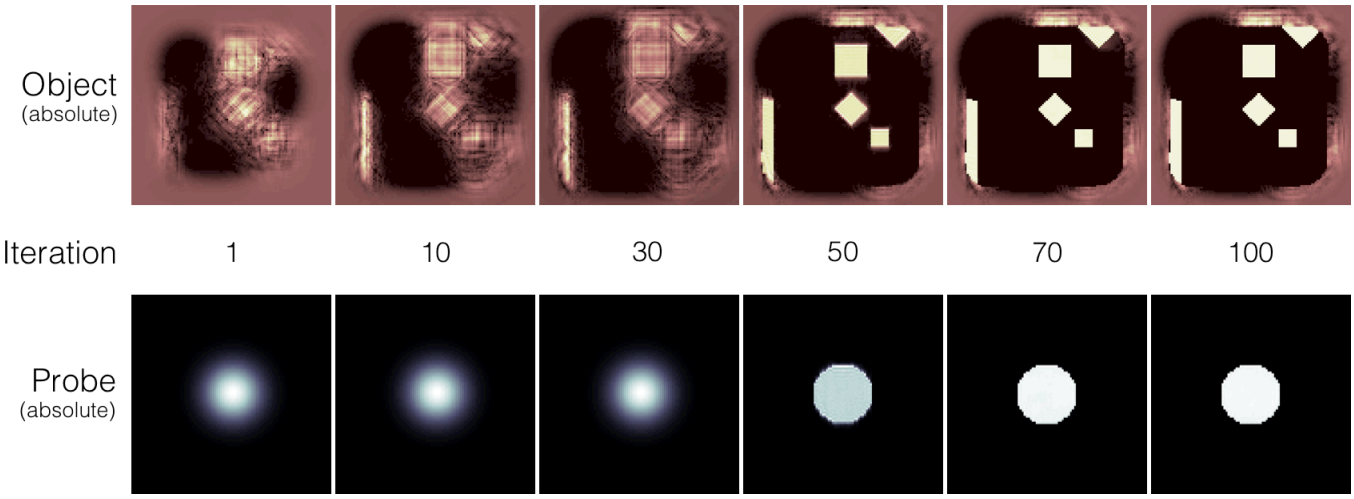

Figure 19: Object and probe reconstructions from the ptychography simulation (absolute values, at the sample plane). The probe is fixed with an initial guess for the first 30 iterations. The object grid is $240\mu m$ by $240\mu m$ and the probe grid is $225\mu m$ by $225\mu m$.

Once the algorithm begins to update the probe guess after 30 iterations the object reconstruction quickly converges to the correct object as shown in Figure 18. The error metric in ptychography may be similarly designed as for the single-diffraction phase retrieval problem. The only difference is that the sum goes over all of the diffraction patterns and all of the sub-object exit waves. Figure 20 shows the error measurement after each iteration.

These results indicate that the simulation generates ptychography data that is capable of being reconstructed. Furthermore the simulation has been extended to allow the probe to be composed of multiple different frequencies of light so that I may simulate hyperspectral data. This simulation both verifies that the desired geometry for my experiment will work and allows me to begin testing the potential of hyperspectral ptychography in simulation.

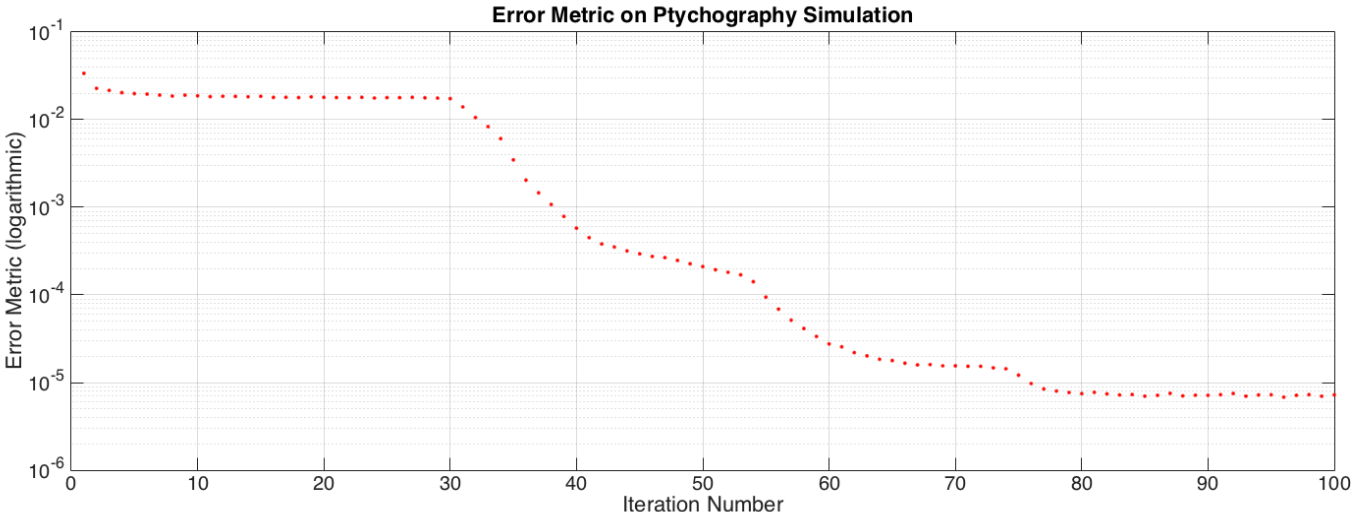

Figure 20: Error measurement from the reconstruction of the simulated ptychography data. For the first 30 iterations the probe is fixed, afterwards the algorithm increasingly converges towards the correct solution.

3.3 Simulated Beam Propagation

Ptychography does not necessarily require the detector to be placed in the far-field. However, the 2D Fourier Transform is a computationally efficient propagator between the diffraction space and the sample space. If one were to place the detector at a different location on the optical track he or she would need to determine the propagation relationship between the two spaces using Helmholtz equation discussed in the background. This third simulation propagates an electromagnetic wave with a given spatial profile. The simulation has two key uses. It can first verify the Fourier relation in the far-field limit for the system, and second it can propagate a recovered probe. This is particularly useful since if the probe does not appear as expected I can propagate it in the simulation to determine if the experiment is misaligned along the optical axis.

The simulation uses the spectral method in order to solve the Helmholtz partial differential equation numerically (equations from[9]),

$$\nabla^2 E = -k^2 E \quad , \qquad E(x, y, z = 0) = P(x, y)$$

which takes the Fourier transform of the wave in the transverse coordinates x and y ($P(x, y)$ is the initial probe). This renders the modified PDE in the Fourier space

$$-(2\pi)^2 u^2 \mathcal{F}[E] - (2\pi)^2 v^2 \mathcal{F}[E] - \mathcal{F}[\partial_z^2 E] \;=\; -k^2 \mathcal{F}[E]$$

that ultimately renders a linear ordinary differential equation,

$$\frac{\partial^2 \Psi}{\partial z^2} \;=\; \left(k^2 - (2\pi)^2 (u^2 + v^2) \right) \Psi$$

where $\Psi = \mathcal{F}[E]$. The solution to the ODE is $\Psi = \Psi_0 e^{-\alpha z}$ including $\alpha^2 = (2\pi)^2(u^2 + v^2) - k^2$ as a Fourier equation parameter. This constant function in front of the exponential is independent of z, but still dependent on the spatial frequency variables u and v. The initial condition (the probe) may be used to identify this constant function $\Psi_0 = \mathcal{F}[P(x, y)]$. The final propagation solution calculated by the simulation is

$$E(x, y, z) \;=\; \mathcal{F}^{-1}\Big[\; \mathcal{F}[P(x, y)]\; e^{-\alpha\; z} \;\Big]$$

To test the success of my simulation I create a Gaussian beam with a waist of $w_0 = 150\mu m$ and translate the beam back a distance of 8.84 mm from its tightest focus. This distance is the Rayleigh range of the beam, meaning that the Gaussian envelope of the beam as a radius that is $\sqrt{2}$ times its beam waist. Figure 21 illustrates how the envelope of a Gaussian beam evolves during propagation.

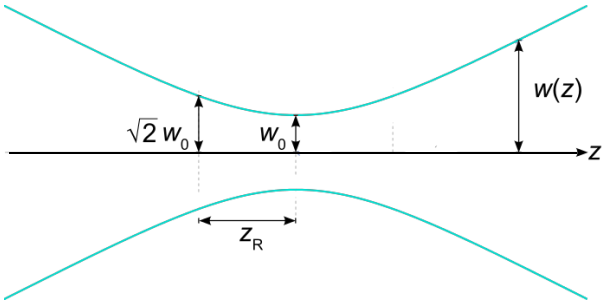

Figure 21: Illustration of how the envelope of a Gaussian beam evolves during propagation. w_0 is the beam waist of the wave, $w(z)$ is the beam radius as a function of its position along the optical axis, and z_R is the Rayleigh range of the beam.

The blue curves show the beam's envelope where the intensity of the beam drops to $1/e$ of its maximum intensity. In the simulation I use a Gaussian beam translated back by its Rayleigh range as the probe as propagate it out two times the Rayleigh range. If the program propagates the beam correctly it should appear identical at the end and have a radius that is reduced by $\sqrt{2}$ in the center. This figure shows the beam at three locations along the axis:

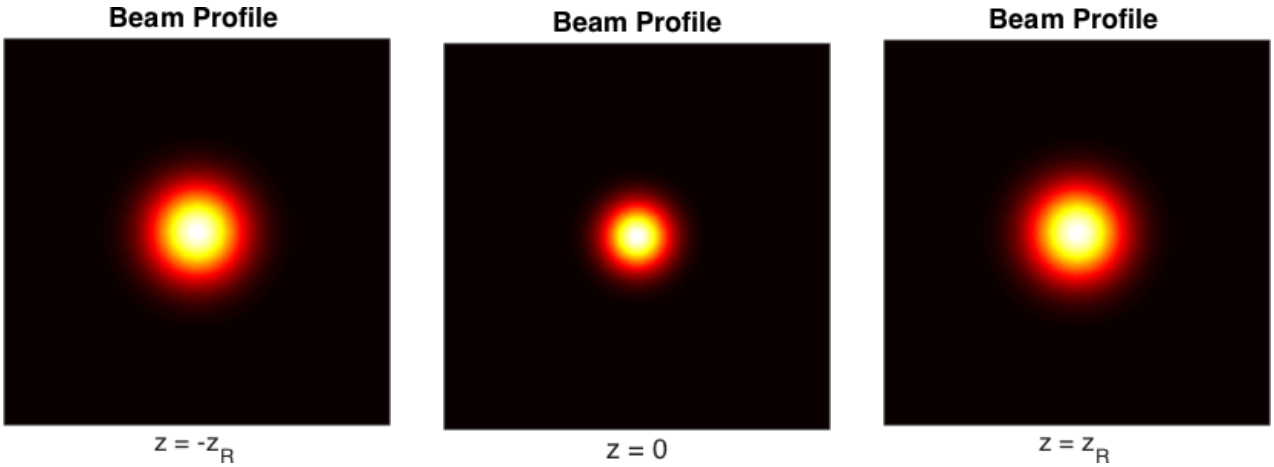

(a) Initial Probe $z_0 = -8.84$ mm (b) Propagated wave to $z = 0$ mm (c) Propagated wave to $z = 8.84$ mm

Figure 22: Three different captures from the beam propagation code. The initial wave is located in panel (a), and the other two panels represent the beam after propagation along the optical axis z. These grids are 1.8mm by 1.8mm.

Evidently the propagation code successfully models a Gaussian beam as the beam returns to the exact state after propagating twice the Rayleigh range. Furthermore at the focus (Subfigure 22b) the radius of the beam is reduced by $\sqrt{2}$ from the radius at the two Rayleigh ranges. A line-out of the propagation is shown in Figure 23.

This figure of the propagation matches with the theoretical Gaussian beam envelope shown in Figure 21. The simulation uses lengths approximately matching with the physical lengths of the beam in the ptychography prototype for single color ptychography (red diode laser, 657nm wavelength probe).

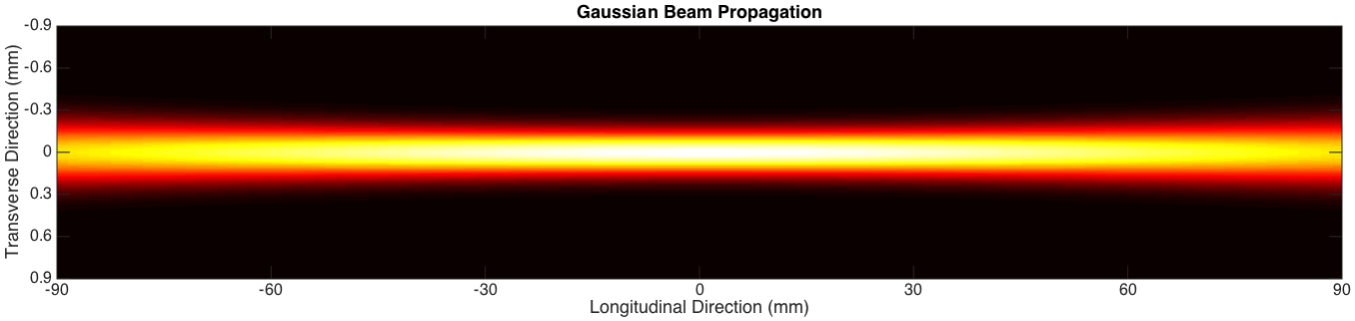

Figure 23: Line-out plot of the beam propagation. The simulation uses lengths approximately matching with the physical lengths of the beam in the ptychography prototype.

To show the extended application of the propagation program to debugging the geometry of the experiment, I show a reconstruction of the probe from a ptychography scan using a blue laser diode of $\lambda = 450$nm for the illumination. Figure 24 compares the reconstructed probe with the simulated back-propagation of the probe. The expected probe was a flat, circular aperture with a diameter of roughly 150 microns. The ptychographic reconstruction showed that the probe was not as expected, featuring some slower intensity decay around the edges.

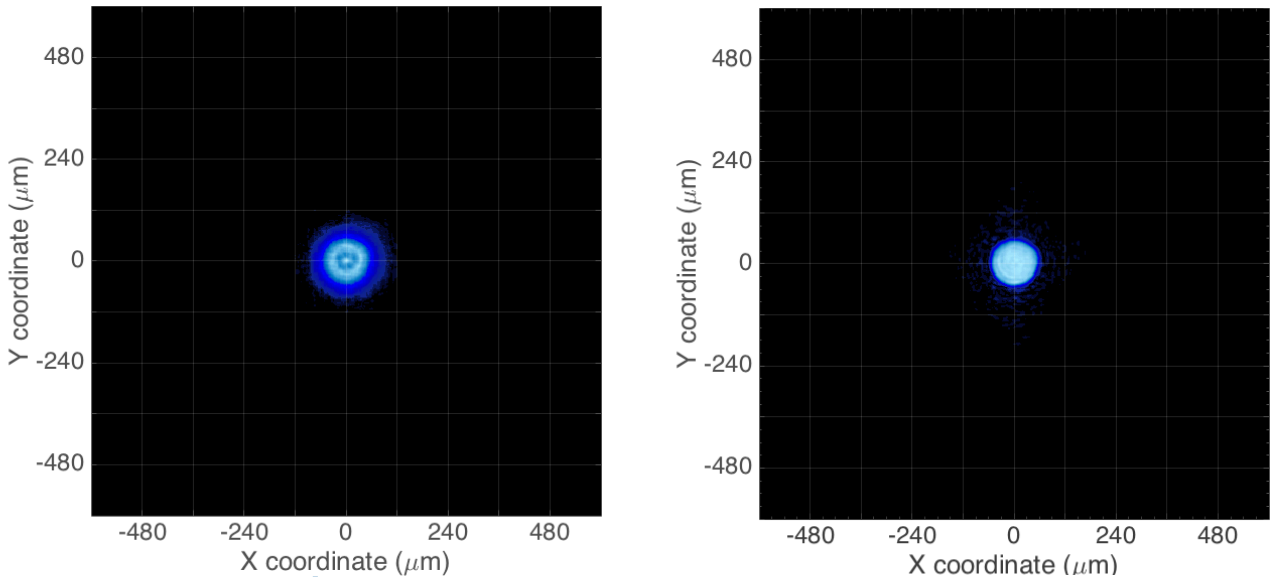

(a) Initial probe from a ptychographic reconstruction

(b) Back propagated probe by 1.08mm via simulation.

Figure 24: Application of beam propagation code showing the reconstructed probe from a blue ($\lambda = 450nm$) diode laser ptychography scan (panel (a)) along side the probe propagated backwards by 4.2mm (panel (b)).

The sample plane is shifted from the correct position by 4.2mm. In fact, the probe reaches its tightest focus with a radius of 75 microns after back propagating 4.2mm, also the beam attains its hard edge at this position on the optical axis that is expected from the circular aperture used to form the probe. This misalignment in the experiment may be adjusted by translating the sample plane backwards on the optical axis, towards the imaging lens.

4 Experimental Assembly

4.1 Optical Apparatus

Microscopy aims to produce an image of a sample with high resolution and relatively little damage to the sample. Traditional transmission microscopes accomplish this by first illuminating the sample and then mapping the transmitted light using an imaging lens. While it is evident that that this technique does not extend into the smaller spatial regime due to a lack of optics in the EUV region, the transmitted diffraction pattern may be sufficient for reconstructing the sample provided that the probe is coherent. In practice this EUV source may be produced using HHG. The objective of my project is to demonstrate the potential of hyper-spectral ptychography by prototyping[16] new forms of ptychography in the visible spectrum. Producing a coherent visible probe requires multiple stages between the laser source and the sample including a spatial filtering, position alignment, angle alignment, collimation, and imaging stage. Additionally a transform lens is necessary directly behind the sample in order to guarantee that the detector exists in the far field. The full experimental apparatus is shown below for two-color ptychography.

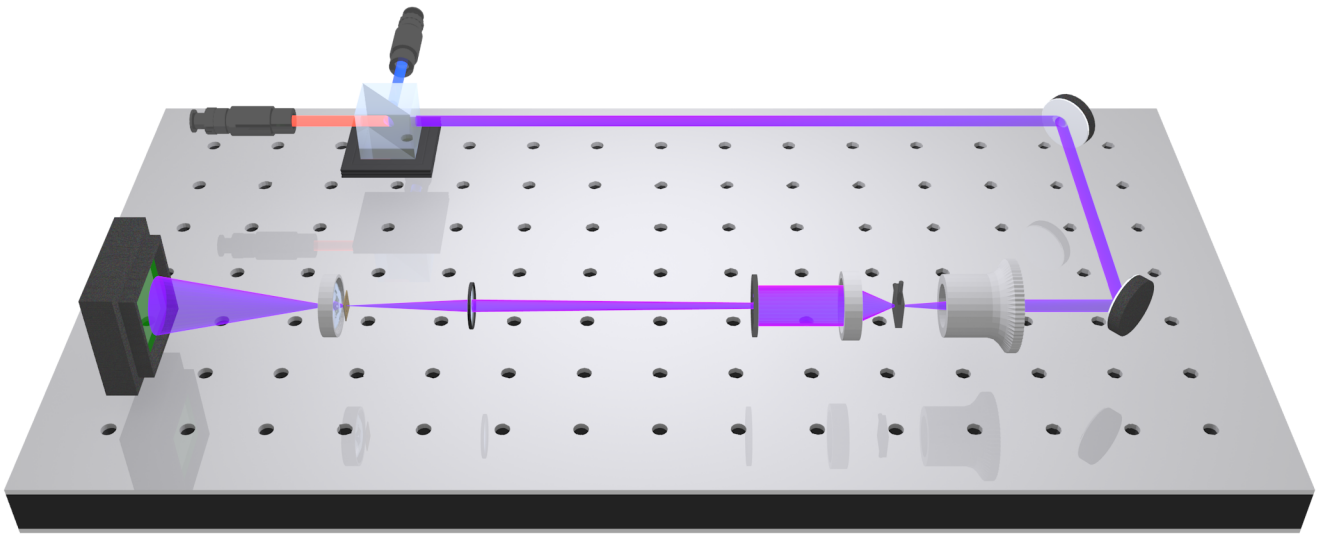

Figure 25: Full apparatus for two-color ptychography. Two laser diodes feed into a beam splitter that combines the beams. Afterwards the multiplexed beam is spatially filtered and formed into a circular aperture that gets mapped onto a sample. The illuminated sample transmits a diffraction onto the CMOS detector.

The source is first aligned into the spatial filter, which outputs a coherent planar wave. The source may have multiple spatial modes. After passing through the spatial filter the beam is monochromatic with a 00-spatial Gaussian mode, which is accomplished this decomposing the input beam into its spatial frequencies. Only the constant mode is located at the center of the beam after one focal length of the lens. The aperture simply crops out all other spatial frequencies. Choosing a tighter filter emits a more planar wave, but reduces the brightness of the output beam. Alternatively a larger filter maintains brightness, but emits a less filtered beam. For this experiment the filter has a 5μm diameter aperture.

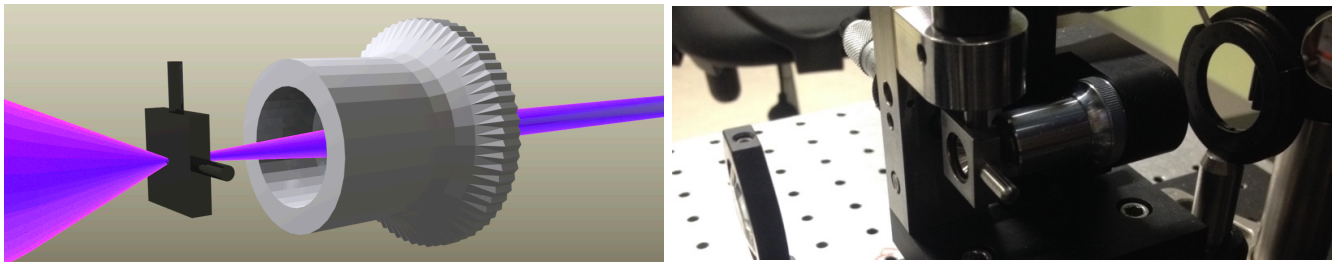

(a) Render of spatial filter.

(b) Photograph of spatial filter.

Figure 26: Spatial filter stage. Newport, 900: with 5 μm pinhole 900PH-5 and M-10X objective. The left optic (of Subfigure 26a) tightly focuses the beam from the source. This beam is focused to the location of the spatial filter (black optic right). Thus the output probe is spatially filtered such that the emitted probe is a planar wave. Subfigure 26b shows the spatial filter stage in the experiment.

The tolerance of the filter is dependent on the size of the aperture. A large aperture will provide minimal filtering on the beam while a small aperture will finely filter the beam at the expensive of the beam's power. After exiting the spatial filter the probe diverges. To correct the rapid beam divergence after the spatial filter it is necessary to include a collimating lens as shown in Figure 27 below.

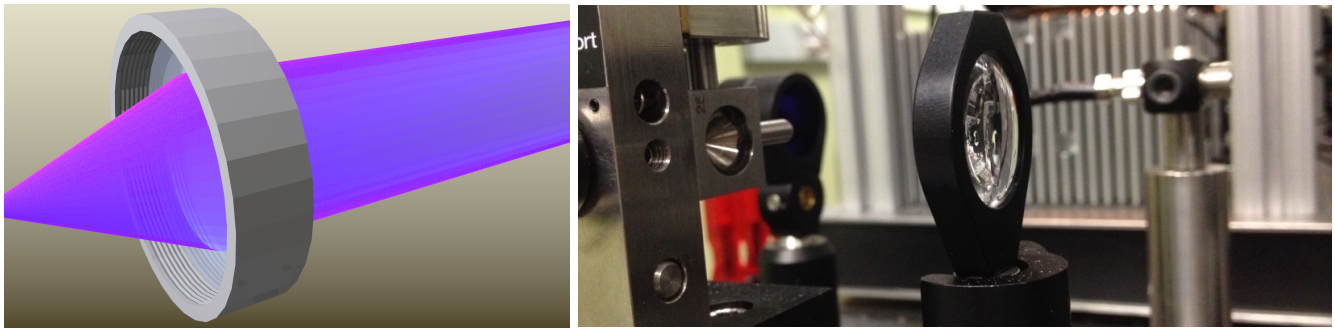

(a) Render of collimating lens.

(b) Photograph of collimating lens.

Figure 27: Collimating stage of the apparatus. The probe exiting the spatial filter is collimated using a convex lens. Aligning the collimation stage is accomplished by reflecting the light a far distance from the optic and comparing the beam size both in the near and far region. Subfigure 27a shows a 3D rendering of the beam passing through the collimating lens. Subfigure 27b is a photograph of the collimating lens in the experiment.

The collimating lens is 1 inch in diameter with a focal length of 5cm. By fine tuning the position of the lens along the beam path, the exiting probe may be collimated such that its size remains constant an arbitrary distance from the optic. Experimentally this is accomplished by arranging a long optical track for the beam to travel, then observing the profile of the beam along the track and making positional adjustments on the collimating lens until the profile appears uniform. It is necessary to collimate the beam because it provides the experimenter control over the size of the beam. Although this optical geometry does not allow any freedom in the size of the collimated beam (which is fixed by the spatial filter and the focal length of the collimating lens) a collimated beam prepares the beam for the imaging lens to map a desired probe onto the sample. Following the collimating lens is the pinhole.

For the visible tabletop ptychography prototype this pinhole is a circle with 300μm diameter. Yet after exiting the pinhole the beam is no longer collimated, so to map the pinhole onto the sample at a smaller scale it is necessary to place convex lens between the sample and the pinhole. This lens images an inverted, scaled copy of the aperture onto the sample under the following equations

$$\frac{1}{f} = \frac{1}{d_i} + \frac{1}{d_o} \qquad M = -\frac{d_i}{d_o}$$

where f is the focal length of the imaging lens, d_i is the distance from the lens to the sample, d_o is the

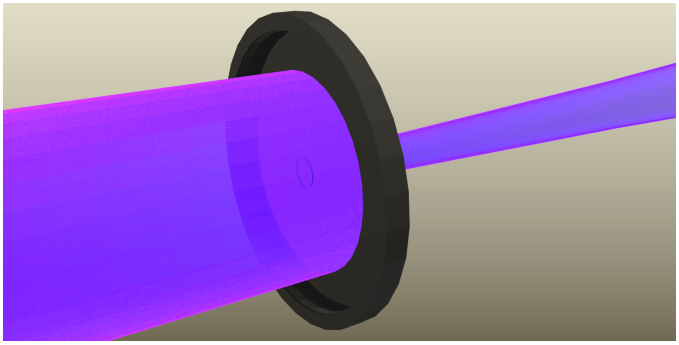

Figure 28: Pinhole stage. The pinhole determines the profile of the probe that will be mapped onto the sample. Ultimately the aperture will be demagnified to be appropriate for the sample.

distance from the pinhole to the lens, and M is the magnification of the pinhole. The negative sign associated with the right equation indicates the inversion on the image. Fortunately, the aperture is symmetric so the inversion has no effect on the imaging. A visual representation of the imaging equation is illustrated by Figure 29 showing a convex lens (center) mapping the green object (left) to the inverted green image on the right.

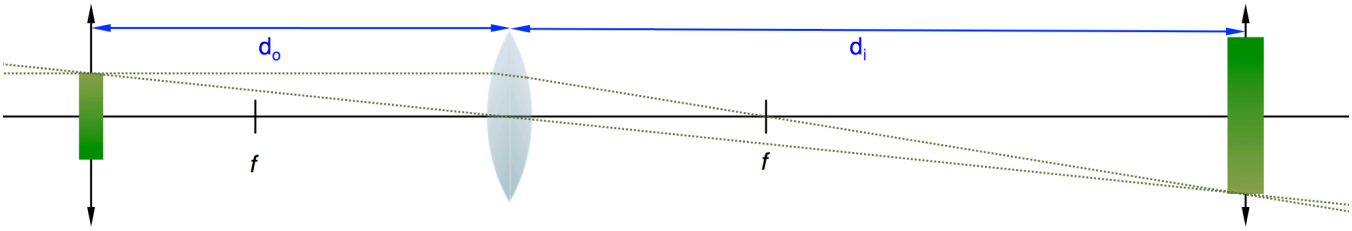

Figure 29: Visualization of the imaging equation. The green object on the left represents the pinhole and is imaged by the convex lens to the green image on the right. The coloration on the object reveals how the lens inverts the object. If the lens is closer to the object than the image then the image will appear magnified, but in the experiment it is desired to demagnify the pinhole so that the lens is closer to the image.

Figure 29 shows how a convex lens may magnify an object. Considering the top of the object as a point source, the light traces from this point must converge to the equivalent point in the image. Only two ray traces are revealed in the figure; one ray travels initially parallel to the beam axis (so that the lens corrects this ray to its focal point), and the other travels through the center of the lens. Figure 30 shows the optical geometry of the imaging lens in the experiment.

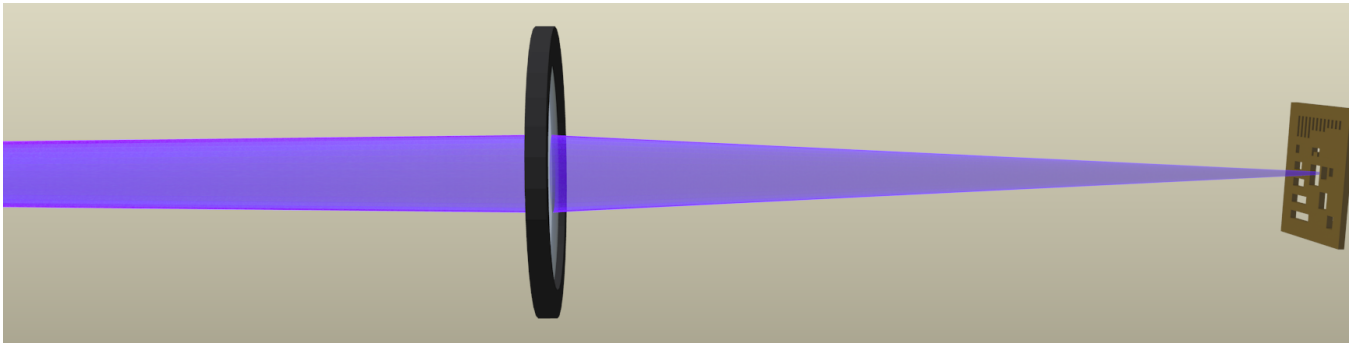

Figure 30: Imaging stage. A convex lens (center) exists between the pinhole and the sample (right) so that the pinhole may be demagnified and mapped onto the sample. This aperture is inverted onto the sample, yet this is inconsequential due to the axial symmetry of the beam.

In order to demagnify the image of the circle $|M| < 1$ it is necessary for the pinhole-to-lens optical arm to be longer than that of the lens-to-sample arm. In the optical ptychography prototype the imaged probe onto the sample is approximately $75\mu m$ so this required that $d_o = 4\ d_i$. The two constraints on the system are the demagnification value $|M| = \frac{1}{4}$ and the focal length of the lens $f = 2.0cm$. Since there are two known variables and two equations the solution to this problem exists, and the distances are $d_o = 2.5cm$ and $d_i = 10cm$.

Once the sample is illuminated it is necessary to have a method of capturing the diffraction pattern. As covered in the Background, the far-field limit for Fraunhofer diffraction is achieved if $z >> \frac{\pi}{\lambda}(x^2 + y^2)$. The value of $x^2 + y^2$ is the squared radius of the imaged pinhole, which is $r^2 = 1.4 \times 10^{-9}\ m^2$. With a wavelength of 600nm the far-field condition must be $z >> 7.4mm$. The maximum allowable range to achieve a reasonable numerical aperture would be 30mm, which just meets the condition. For EUV sources the far-field condition is easier to satisfy not because of its frequency, but because the probe's diameter is smaller by multiple orders of magnitude. In the optical regime however, the far-field condition is not guaranteed.

To make the prototype more adaptable to changes in the probe a transform lens is placed just after the sample. A consequence of Fourier optics is that the Fourier transform of the exit wave from a convex lens appears exactly one focal length away from the lens, so it is possible to create the same conditions of the far-field limit closer to the sample using a lens. This seems paradoxical as traditional optical microscopes implement a lens beyond the sample in order to attain a direct image. Furthermore CDI is a lensless imaging technique. However, one of the advantages of CDI is its ability to extend into the extreme Ultra-Violet and soft X-ray regime for an increased spatial resolution. Although a lens between the sample and the detector is used to achieve the far-field limit in the optical ptychography prototype, this lens simulates the conditions of EUV CDI where the diffraction reaches far-field limit in a significantly shorter distance.

Figure 31 depicts the final stage of the optical ptychography prototype in which the exit wave from the sample strikes the transform lens and diffracts onto the CCD detector one focal length away.

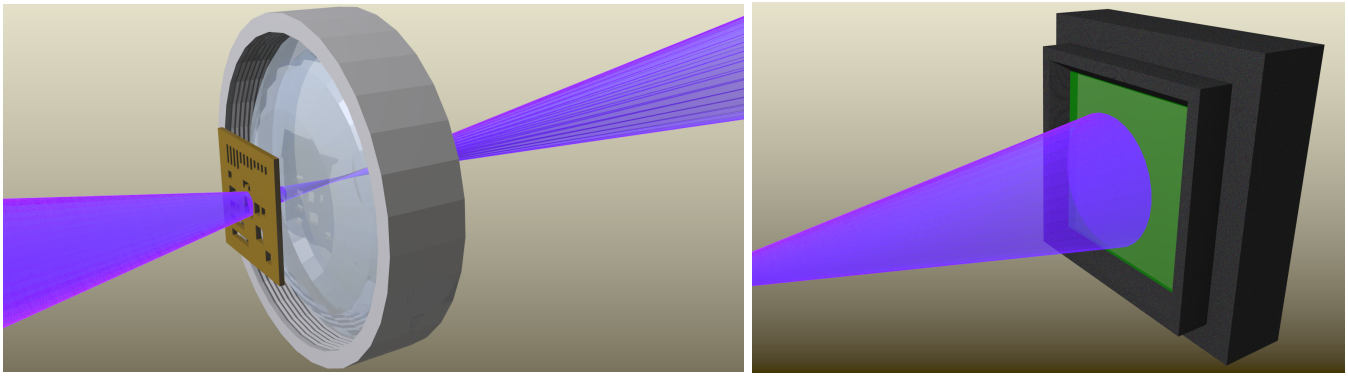

(a) Transform Stage

(b) Diffraction stage

Figure 31: A convex lens labeled the *transform* lens is placed directly after the sample along the beam line. The transmitted exit wave from the sample immediately passes through the transform lens and emits onto the CCD detector.

With the transform lens and sample so close to one another the propagation from the sample to the lens is negligible so the reconstruction of the exit wave matches the exit wave from the sample. Though exhaustive, this optical geometry guarantees that the propagator between the sample and the diffraction is the Fourier transform and it guarantees that the probe is coherent. Additionally this geometry allows for manipulation of the probe's shape and size based on the imaging relation and the pinhole.

Two PI stages (not shown in Figure 31) are used to translate the sample in the transverse directions. Instead of scanning the probe along the sample to collect data, the sample is attached to an arm that moves transversely to the optical axis. This choice has a few advantages over shifting the probe. The geometry required to create a system that could actively shift the optical path using a computer would be rather challenging. Likely this would require the use of piezo electric optical components. Also the shifting the probe could possibly compromise the uniformity of the beam between scan positions so that slightly different probes illuminated different regions. Additionally the detector would need to be moved with the probe so that the camera was centered about the optical axis.

So to complete the assembly I needed to find a way to move the sample electronically. The experiment not only required me to acquire and align this optical geometry, but it also required me to write a program so that the PI stages and the CMOS Mightex USB 2.0 detector worked cooperatively to collect the ptychography data. This programming is further discussed in the code section below.

4.2 Experiment Software

To collect ptychography data it is necessary to have a detector that can capture the far-field diffraction pattern and to have translation stages that can scan the position of the sample on the probe. As noted in the Optical Apparatus section the sample is translated for each scan rather than the probe. An optimal system would include a fully comprehensive program that controlled both the detector and the translation stages so that with a single click the camera would capture a diffraction pattern, the sample would translate a known amount, the camera would capture another diffraction, and the program would continue to record the diffractions for each position in a specified scan grid.

For detection I used a Mightex USB 2.0 CMOS camera (which provided SDKs for LabView, Visual Studio C#, and Matlab) and for translation I used two PI Mercury DC motor controllers (due to availability one stage was a C-862 model and the other was a C-863 model). With three separate devices, it became a significant challenge to create a program that controlled everything. After attempting to pursue coding in multiple programs, the most compatible program for the devices was found to be Matlab. They all required different *.dll* files to operate, but were all compatible with 32bit Matlab on Windows 7 via USB connections. The two PI stages were similar, yet not identical in function. Fortunately they could daisy chain together so that only two inputs were connected to the camera; one USB connection for the Mightex camera and another USB connection for both PI stages. The Graphical User Interface (GUI) for the Matlab program to collect ptychography data on the optical prototype is shown in Figure 32 below.

The program operates primarily in two different modes. The first mode is an active mode in which the user can control the devices manually and see results in real time. The other mode is a scan mode that engages when the user presses the "Start scan!" button after finalizing the details of the ptychography scan. This mode visits each specified scan position in the grid and captures a diffraction pattern. Before taking a scan I need to specify the step-size taken by the sample, the size of the scan grid, the central location of the scanning area on the sample, the number of accumulations, and the randomness in the scan positions (as noted earlier the ptychographic algorithm prefers less symmetry in the scanning grid).

In the active mode I have control of the parameters for the scan. A key part in preparing a scan is identifying the central region that you wish to scan on the sample using the stages. I arranged the PI stage controllers orthogonal to each other so that the first axis controls horizontal motion (x axis) and the other controls the vertical motion (y axis). These stages translate position by revolving about a finely threaded rod, so step sizes are provided in units of eighth-revolutions, or counts, rather than length. This presented

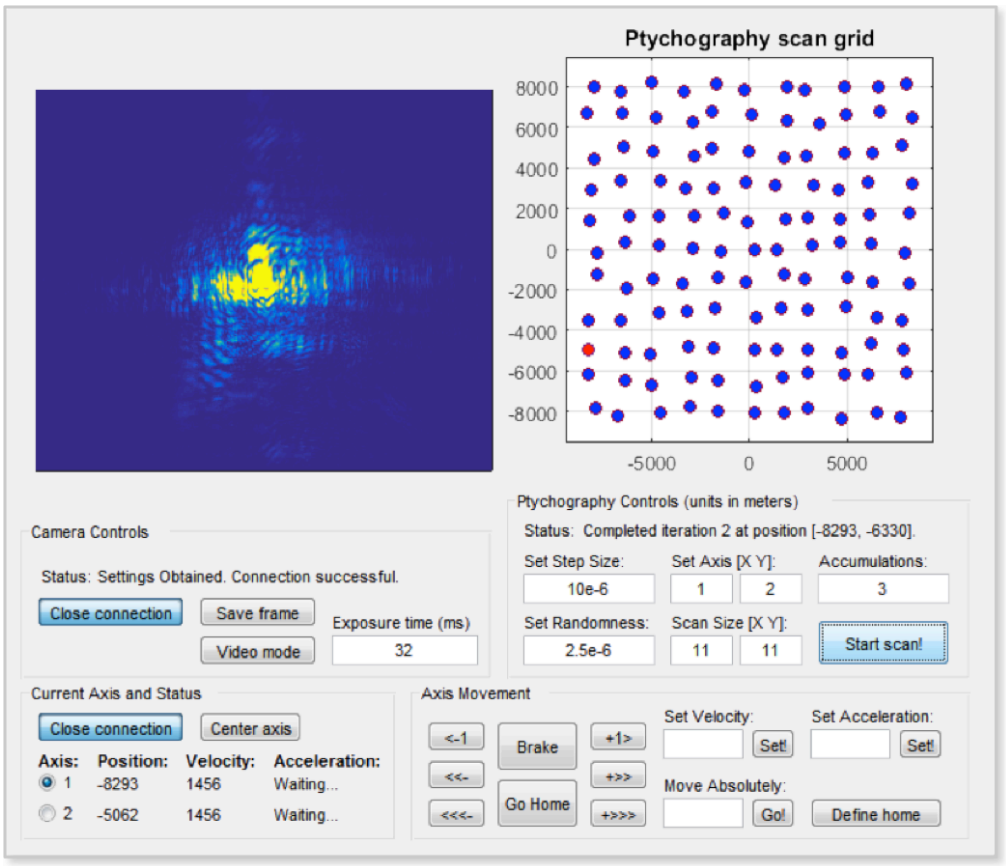

Figure 32: Graphical user interface developed in Matlab for collecting ptychography data. The upper left image provides a real-time display of the diffraction pattern being record while the upper right shows the scan grid in units of PI stage steps (The red dot indicates current relative scan position). The interface on the bottom half allows for manipulation of the ptychography settings, including step sizes, scan area, and accumulations.

the requirement for a conversion between the two measurements of travel, which was found to be 4.8nm per count. These stages offered additional functionality that allowed for velocity and acceleration input for the stage motion, shown in the bottom left of Figure 32. Under the axis movement panel I can step in either direction by a single step, 50,000 counts, or 200,000 counts. I can also specify an absolute location to travel to as well as define a new home for relative motion.

Under the camera controls panel I can either view the real-time image from the camera or view a freeze frame from the camera by toggling the "video mode" button. The exposure time dialog box allows me to specify the time for exposure to the camera between frame captures during the real-time viewing. This exposure value is only for temporary viewing and is not used in scan mode. If desired I can capture the current frame using the "save frame" button. This is a convenient feature for single-diffraction CDI and is beneficial for a manual ptychography scan if the scan mode is not running successfully.

The final feature to specify is the accumulations value under the ptychography controls panel. The Mightex camera stores the diffraction patterns using discrete units on a byte scale (0,255). If the intensity of the light reaching a pixel is insufficient for a given exposure time to be detected, then the camera will not register any light at this point in the diffraction. On the other hand a pixel may be over-saturated if too much light is received for a given exposure time. Furthermore the pixel does not react linearly with the intensity when near the pixel saturation. In order to acquire a more finely discretized diffraction that neither experiences under-saturation or over-saturation multiple captures are taken at a position with multiple exposure times; the number of captures is specified by the accumulations value. Figure 33 shows

the multiple diffractions collected at a single position with varying exposures.

The capture with the largest exposure time (panel 33a) successfully detects a lot of crucial diffraction

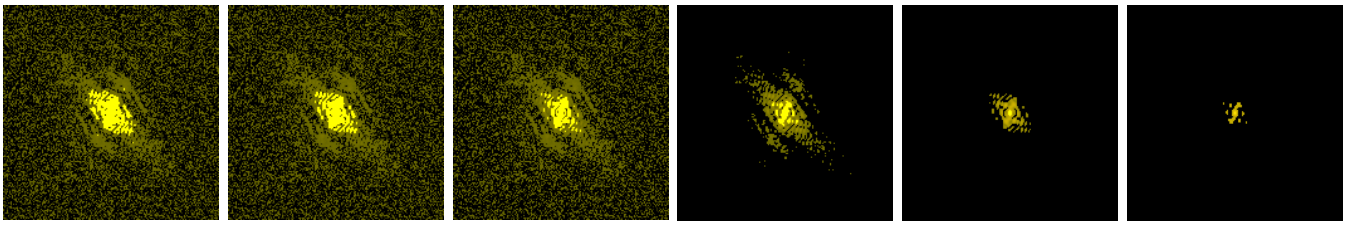

(a) 100ms exposure. (b) 90ms exposure. (c) 80ms exposure. (d) 40ms exposure. (e) 3ms exposure. (f) 400us exposure.

Figure 33: Six identical diffraction intensities measured by the Mightex CMOS detector with varying exposure times. The camera stores the data using bytes ranging [0,255] so to attain a more finely discretized diffraction pattern it is necessary to *dynamically range* the data. Intensity patterns are on a $5.24mm \times 5.24mm$ grid.

data out from the origin, but over-saturates near the center. Conversely the shortest exposed capture (panel 33f) recorded the central peak of the diffraction without over-saturating at the expense of failing to detect light farther from the origin. So to build a full diffraction I wrote a program to dynamically range the recording. Dynamic ranging stitches together the appropriate parts of each capture to create a single diffraction that covers the entire range of intensities bypassing the byte's discretizing unit.

The program first takes the capture with the largest exposure (in this experiment the largest exposure time is $100ms$) and creates a mask of the area in which the pixels do not exceed the saturation level (mask shown in Subfigure 34a). Next the program creates a mask of the remaining space, then it moves to the next longest exposure time ($90ms$) and generates a mask of all appropriate pixels that do not exceed saturation and are in the mask of the remaining space (shown in panel 34b). This masking technique continues until the capture with the shortest exposure time ($400\mu s$) in which the final remaining mask is filled entirely by this final capture, which is I make sure is never over-saturated. At each stage the new addition to the full diffraction is normalized by the exposure time.

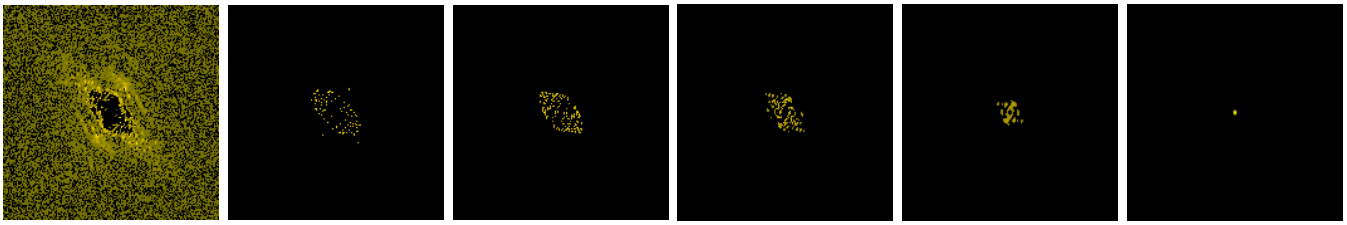

(a) 100ms mask. (b) 90ms mask. (c) 80ms mask. (d) 40ms mask. (e) 3ms mask. (f) 400us mask.

Figure 34: The generated masks of each frame capture for dynamic ranging. These masks select pixels within the linear region of the detector (so byte values that are less than 190) from each capture, and then are combined to form the full diffraction pattern. Grids are $5.24mm \times 5.24mm$.

The exposure times used in the ptychography scan program depend on the transmission of the sample being imaged and the intensity of the illumination. Initially the ptychographic scans used 15 accumulations, but it was later found that only 3 accumulations were necessary to sweep the range of intensity values for the diffraction. The Mightex CMOS detector could vary its exposure time from $750ms$ to as short as $50\mu s$, yet the camera provided undesired features on the captured frame for exposure times below $100\mu s$.

The optical geometry allows for manipulation of both the choice of illumination source and of the spatial profile of the probe, which will be useful for fulfilling the purpose of this prototype. First I collect a single diffraction pattern from an aluminum sample with a shape cut into the metal plate using a large red ($\lambda = 657nm$) beam (the imaging lens is set for a demagnification of $M = 1$, so the probe is $300\mu m$ in diameter) to test single-diffraction CDI. Then I move to take a ptychographic scan of the United States Air

force (USAF) sample using the red diode laser ($\lambda = 657nm$) with a smaller diameter ($75\mu m$). From there the ptychography prototype is put to the test via two-color ptychography using red and blue (450nm) laser diodes, then two-color ptychography using a red diode laser and a Helium-Neon laser ($\lambda = 633nm$), then ultimately hyper-spectral ptychographic using broad bandwidth illumination.

5 Results

The main objective of the optical tabletop ptychography prototype is to test the merit of hyper-spectral ptychography using a broad bandwidth source for the illumination. Ptychographic imaging from a broad bandwidth source has direct application on the EUV ptychography experiment using the full spectrum produced by a HHG source. In this section I share the results from multiple different experiments conducted using this prototype, ranging from the initial tests with single-diffraction CDI to Mutual Incoherence Ptychography.

5.1 Single-Diffraction CDI

Testing if the experiment could collect ptychography data by reconstructing an image from a single diffraction pattern was an invaluable step for me to verify that the apparatus was correctly assembled. The successful reconstruction confirmed that the red diode laser passing through the spatial filter was a coherent source of illumination. Furthermore it confirmed that I had satisfied the oversampling conditions necessary to image the sample and that the detector was positioned exactly one focal length from the transform lens.

The sample for this experiment is a thin aluminum sheet with a few geometric shapes cut out (Figure 35). The negative region stretches about 150 microns across the plate, so to fully image the pattern with the probe I moved the imaging lens so that the pinhole mapped directly onto the sample with a diameter of 300 microns. So the imaging lens needed to be moved so that the pinhole-lens arm and the lens-sample arms were equal and two focal lengths of the lens.

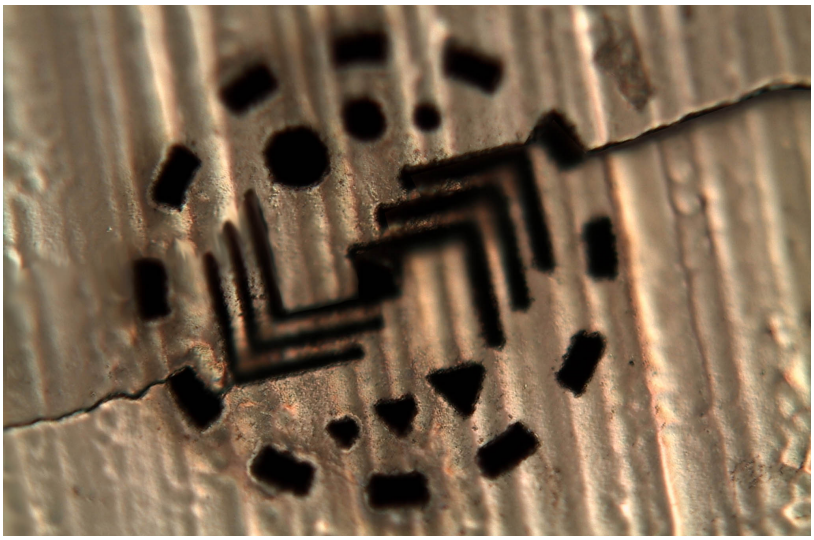

Figure 35: Image recorded using a $50,000x$ object microscope of the sample used to first test the prototype via single-diffraction CDI. The sample is a thin aluminum sheet with cut out geometric patterns. Prior to imaging the sample sustained a large tear though the center of the geometric features. Image is 230 microns across and 170 microns down.

Notably I did not know that the sample had a large tear through the center of the sample until after reconstructing the image. The tear suggests that the two halves are on slightly different planes, challenging the assumption that the exit wave in CDI is flat (this spaced-planes effect can be seen by the non-uniform focus of the image in Figure 35). For the experiment the propagation distance to the detector was $20mm$ and the wavelength of light was $\lambda = 657nm$. The Mightex camera captures images using a 1280×1024 pixel chip with pixels that are 5.2 microns in length so that the detector chip is $6.7mm \times 5.3mm$.

Using the iterative method I can take a single diffraction pattern (attained using dynamic ranging) and recover the phase. This is possible because the oversampling without binning is 16.7, which allows for binning by up to 7. For this reconstruction (in Subfigure 36a) I binned the diffraction by 4 and implemented shrink-wrapping with the HIO algorithm.

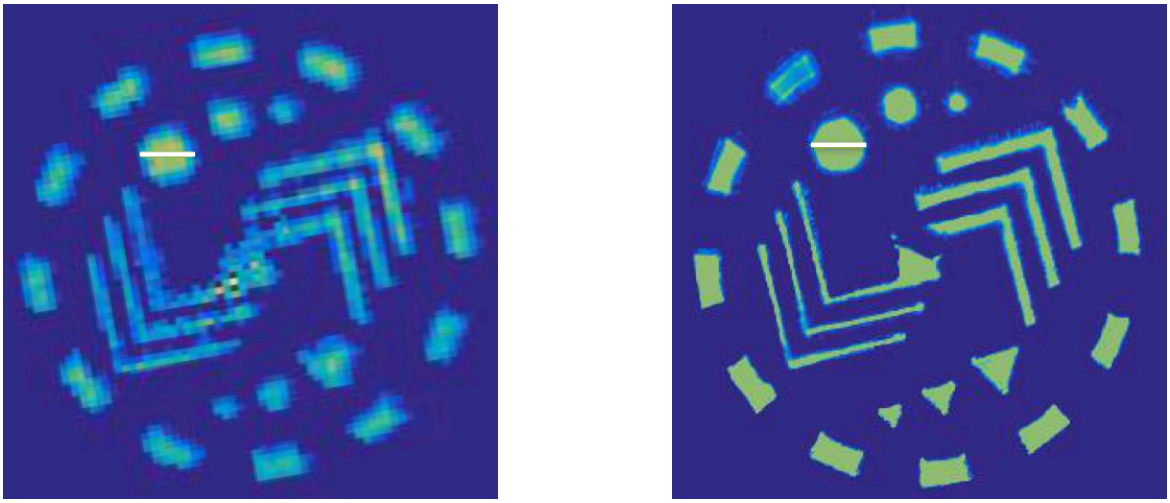

(a) Single-diffraction CDI reconstruction.

(b) Optical microscope image for comparison.

Figure 36: Comparison of the image from single-diffraction CDI to the image from an optical microscope. The white band on each Subfigure is 18 microns.

Given the physical dimensions in the experiment the greatest possible resolution is $R = 2.49\mu m$ resulting from a numerical aperture of $NA = 0.13$. In the sample space each pixel is approximately 2 microns, which comes near the resolution limit, suggesting the reconstruction could reach near-pixel resolution. In this reconstruction I showed that CDI can produce the image of the sample in transmission.

These results are rather exciting because they verify that the prototype is set up correctly for ptychography. It may seem odd that I am building this diffractive imaging microscope since a typical optical high-object microscope seems to achieve a greater spatial resolution. Yet the optical ptychography prototype is not intended to compete with other microscopy techniques for spatial resolution (since ptychography in the EUV achieves superior resolution to optical microscopy); its function is to test new extensions to ptychographic imaging. And now that the microscope collects far-field diffraction patterns the next step is red a single-color ptychography scan.

5.2 Single Frequency Ptychography

The single-diffraction results served a milestone for me that proved the probe was correctly tuned and the detector with dynamic ranging correctly collected the far-field diffraction pattern. This next experiment is another milestone in the prototypes development; a successful ptychographic reconstruction proves that the scanning code correctly collects diffraction patterns in the scanning grid.

The setup for this experiment is modified from the earlier setup only in that the probe is demagnified onto the sample by $M = \frac{1}{4}$ by moving the imagining lens closer towards the sample. Otherwise all of the same relations hold. The resolution limit is still $R = 2.49\mu m$ and the numerical aperture is $NA = 0.13$.

For this experiment a new sample with a large range of features was imaged. The new sample appears a square spiral of bars, known as the United States Air Force (USAF) sample, [Thorlabs]. The design is a thin layer of chromium layered onto a glass substrate, so the thickness of the pattern is very thin, but the glass substrate forces back the transform lens. This causes the algorithm to recover images of probe and object at the plane of the lens rather than the sample plane, yet fortunately this glass layer is relatively thin ($2mm$) so the propagation distance is negligible. Figure 37 shows a reflection image of the sample from an optical microscope.

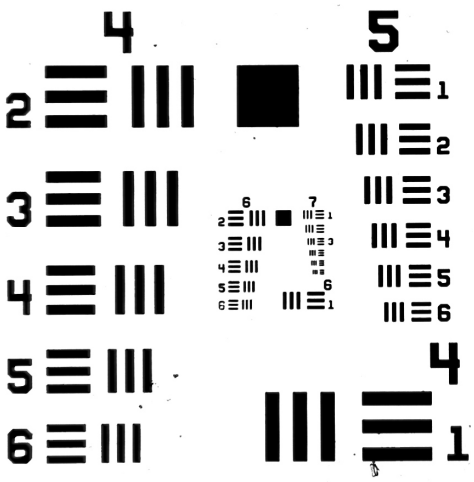

Figure 37: US Air Force Sample imaged in reflection by an optical microscope. The sample is chromium layered onto a glass substrate, and the dimensions of this image are $1.5mm \times 1.5m$.

Similar as with the single-diffraction sample, the USAF sample is mostly reflective with a few various features that transmit light. A benefit of this is that when trying to identify the center of the sample in the ptychography suite I can use the total intensity on the detector to gauge my location. This sample is also particularly convenient because the size of its features range from over millimeters down to $2\mu m$.

The ptychography scan was taken using an 11×11 scan grid with step sizes of approximately $9\mu m$ and a random step of $1\mu m$. Figure 38 shows the reconstructions from the scan, including both the amplitude and phase of the object and probe.

The algorithm successfully reconstructed an image of the scanned region of the sample. Additionally the reconstruction of the probe shows some unexpected properties of the experiment. Instead of being a circular aperture, the probe's amplitude (Subfigure 38) has soft boundaries the *ring* in the radial direction. This behavior is a consequence of sample misalignment, so the sample appears to not be at the correct position along the optical axis. Ptychography is capable of reconstructing an object from a ringing probe, yet a larger probe may challenge the oversampling requirement of the system. The phase for the object and probe may appear rather noisy, but it is only where the amplitude is non-zero that the phase has any significant contribution to the physical object and probe. As expected the phase is constant within the positive regions of the object, and the probe has non-constant phase due to the mis-alignment.

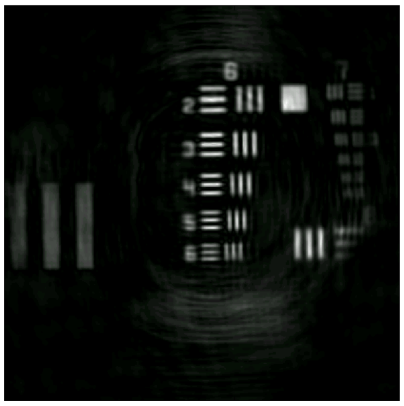

(a) Reconstructed object amplitude.

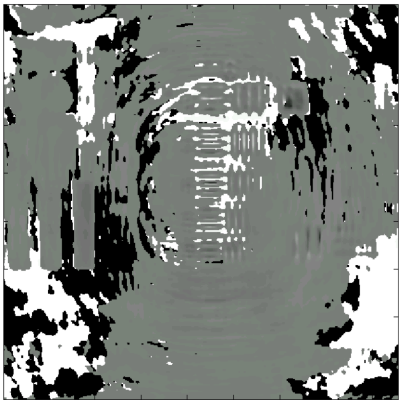

(b) Reconstructed object phase.

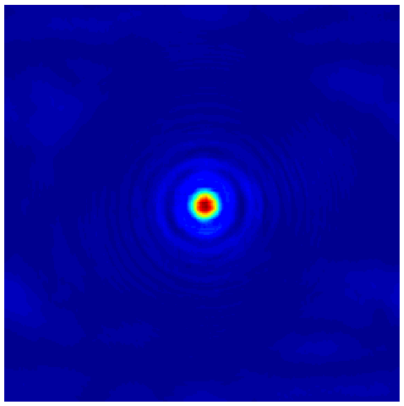

(c) Reconstructed probe amplitude.

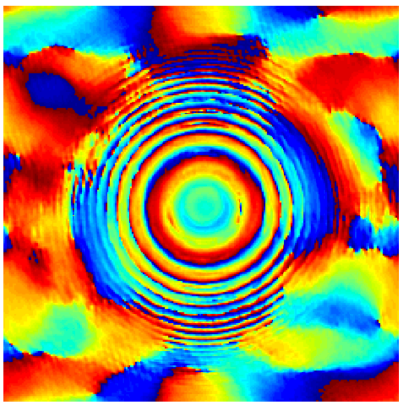

(d) Reconstructed probe phase.

Figure 38: Single-color ptychography reconstructions of the USAF sample using an 11×11 scan grid. Each image is $1.7mm \times 1.7mm$. The reconstructed probe revealed that the probe is not the expected circular aperture, suggesting that the sample is shifted from the imaging position for the lens.

5.3 Red and Blue Laser Ptychography

After demonstrating that the optical prototype could successfully capture ptychography data, I began work on setting up two-color ptychography. The only key difference in the experiment was the alteration to the source by combining the red diode laser with the blue diode laser using a beam splitter. The same USAF is imaged with the same sized probe as before (demagnification of $M = \frac{1}{4}$). One additional factor to consider is the chromatic aberration of the lenses. For most optics the index of refraction depends on the wavelength of the traveling ray, which implies that the alignment for the red laser may not necessarily be sufficient for the blue laser. Fortunately the chromatic aberration is small for the spatial filter and imaging lens, so only a small difference may be detected. The reconstructed probes may provide insight on the effect of the chromatic aberration in the system.

Figure 39 shows the hyper-spectral reconstruction results from a 32×32 scan with $8\mu m$ step sizes. This scan is unique in that the larger scan grid captures both groups 6 and 7 entirely.

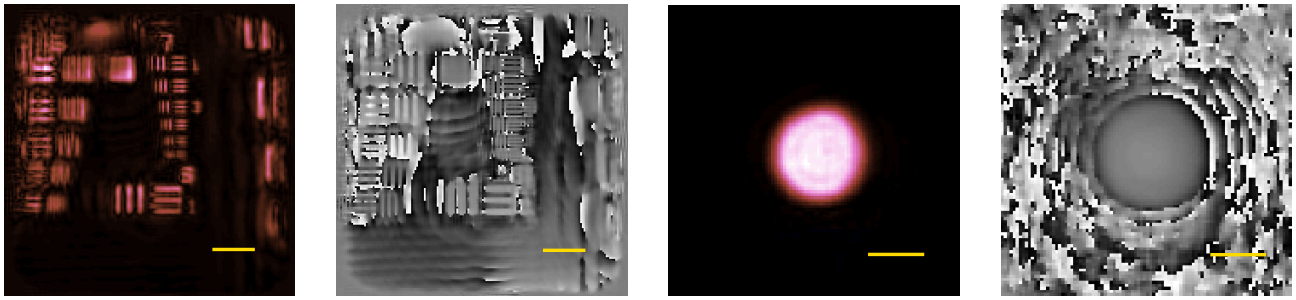

(a) 657nm object amplitude (b) 657nm object phase (c) 657nm probe amplitude (d) 657nm probe phase

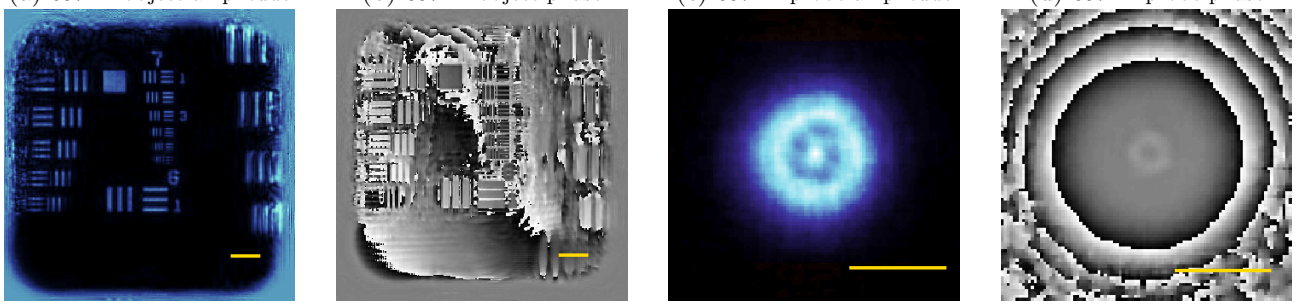

(e) 450nm object amplitude (f) 450nm object phase (g) 450nm probe amplitude (h) 450nm probe phase

Figure 39: Reconstruction results from two-color ptychography. The top row shows the recovered object and probe for the red illumination while the bottom row shows the recovered information for the blue illumination. The sample is the same USAF pattern used in the single ptychography experiment. Gold bars in each image are $50\mu m$.

All of the reconstructions in Figure 39 are consistent with the expected object and probe. Just as with the single-color reconstructions, the phase of each object is approximately constant, or flat, within the positive regions. Group 7 appears to have a small linear phase that could have been caused by a slight tilt in the USAF sample from its normal orientation to the optical axis. Another grand outcome from this reconstruction is the variance of the two probes. Both probes are expected images from the pinhole, yet are unique from each other. This supports that hyper-spectral ptychography authentically solves for two different object-probe pairs rather than simply solving the single-color problem while scaling the guess to the other color.

As anticipated the varying probes indicates that the lenses produce a small degree of chromatic aberration. While the blue probe appears to be imaged perfectly onto the sample, the red probe is slightly out of focus. This suggests that the focal length of the imaging lens varies slightly between visible wavelengths, on the order of roughly a millimeter between the two frequencies.

5.4 Broad Bandwidth Illumination Ptychography

With positive reconstructions in two-color ptychography, the next challenge was to reconstruct the USAF sample using a broad bandwidth source. Just as with two-color ptychography, the modification to the physical experiment is actually not too invasive. Only the illumination source needed to be substituted. Figure 40 illustrates the required modification to the prototype for a broad bandwidth source.

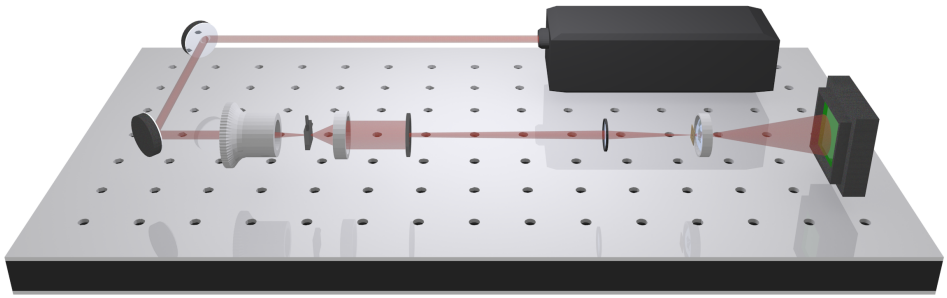

Figure 40: Three-dimensional rendering of the broad bandwidth ptychography experiment. The laser diodes are replaced by a Ti:Sapphire laser which exploits the non-linear behavior of the crystal to generate a Gaussian spectrum in the IR region. The broad bandwidth beam is spatially filtered and formed into a circular aperture that gets mapped onto the NUSAF sample. The illuminated sample transmits a diffraction pattern onto the CMOS detector.

Although the experimental apparatus does not change significantly, there are new elements to consider for hyperspectral ptychography. The multi-color ePIE algorithm not only identifies the object and probe for each specified wavelength, but it can also provide relative spectral weights of the illumination incident upon the sample. Assuming the program successfully identifies the probes for each color, the spectral weight should simply be the sum of the probe pixels for that color.

With the two color experiment I fixed the spectral weights by the measured spectrum of the illumination. Now with the broad bandwidth illumination I allow the algorithm to self-identify the relative weights of the illumination. Using an 11×11 scan grid with the $8\mu m$ step size, I reconstructed the following objects and probes:

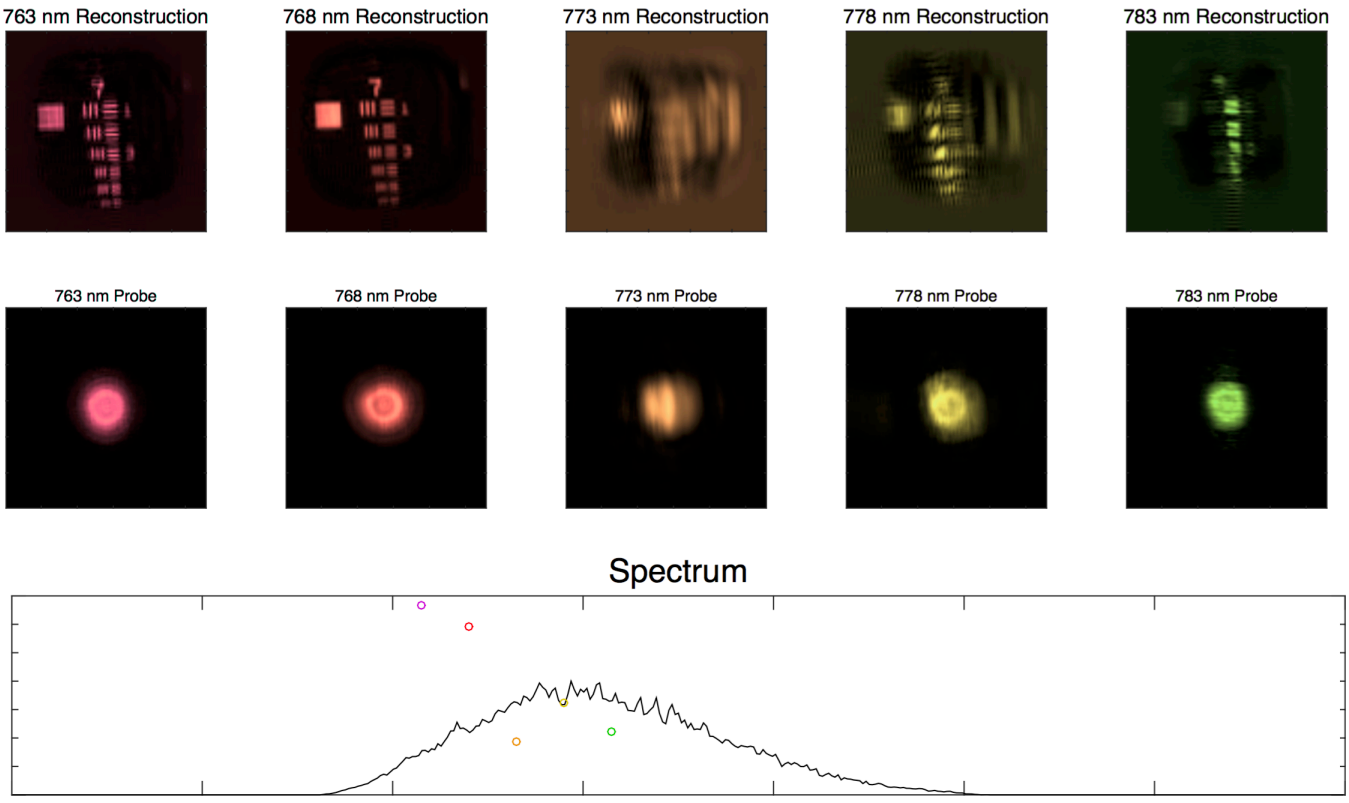

Figure 41: Reconstructions from broad bandwidth illumination ptychography. The reconstructed object and probe amplitudes are color-coded to correspond to the representative spectral weight point on the spectrum plot. The plot has wavelength on the horizontal axis (tick marks are spaced $20nm$ apart, ranging from $720nm$ to $860nm$) and normalized intensity on the vertical axis.

Initial reconstructions of the broadband data indicate that the program has difficulty with discerning the separate frequencies for the Gaussian spectrum. The $763nm$ reconstructed probe and object appear the most finely resolved among the results. There is a correlation between the spectral weight and the quality of the image recovered. Although the probes may vary between wavelengths, the objects should all be approximately uniform (expect for a slight scaling difference) so the blurred reconstructions must not be acquiring the correct image.

It is possible that the probe have a varying spatial profile with wavelength, yet that possibility is less likely as the wavelengths are so close together. Perhaps a new ptychography scan with adjusted step size or randomness could prove easier to reconstruct. Currently I am investigating possible modifications to the ptychography algorithm so that the spectral weights converge to the measured spectrum.

5.5 Mutual Incoherence Ptychography

The principle concept being explored by this optical prototype is the idea of information multiplexing via multiple frequencies. For one ptychographic scan I gain reconstructions for each desired wavelength. This technique relies on the incoherent summing of the different frequencies to for the diffraction pattern. A grander question we asked as a group was "how else can we push the limit of information multiplexing using this idea of mutual incoherence?"

So two novel ideas were attempted in experiment to explore alternate forms of mutual incoherence ptychography. Both experiments physically separated the probe into two different probes. One experiment separated these probes by their wavelength using a diffraction grating and the other experiment separated the probes by their polarization. One significant consequence of the beam separation is that now two different regions of the sample are simultaneously scanned. With these tests we can definitively show that hyper-spectral ptychography reconstructs an authentic image for each probe. With broad bandwidth illumination each probe superimposed each so that they imaged the same region. By altering the beams spatially we can attain unique images for each reconstruction. Each experimental setup is illustrated in Figure 42.

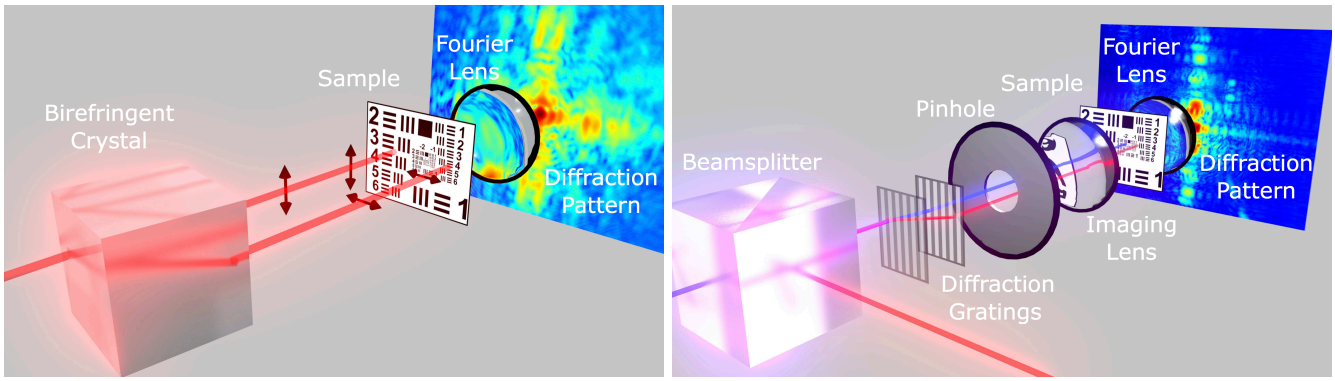

(a) Polarization-split beam geometry

(b) Spectrally-split beam geometry

Figure 42: Figure taken from.[17] Optical prototype modifications for separated beams ptychography. The polarization splitting experiment in Subfigure 42a separates the red ($\lambda = 657nm$) beam by using a birefringent crystal that has an index of refraction dependent on polarization. The spectral splitting experiment in Subfigure 42b separates the red and blue ($\lambda = 450nm$) beams with a diffraction grating that alters the beam paths with respect to each other and with another grating to assure that the beams travel colinearly.

The two experiments alter the later stage of the setup after the spatial filter, as opposed to the two-color and broadband ptychography experiments that altered only the source. For the polarization experiment a red beam is split into two using a barium borate (BBO) crystal, which refracted the light differently for different polarizations and separated the two probes by approximately $216\mu m$. For this experiment a 64-position scan over groups 6 and 7 of the USAF sample was taken. For the spectral splitting experiment two diffraction gratings are positioned after the spatial filter separate the two probes and maintain their collinearity. In the experiment these beams were separated by $175\mu m$.

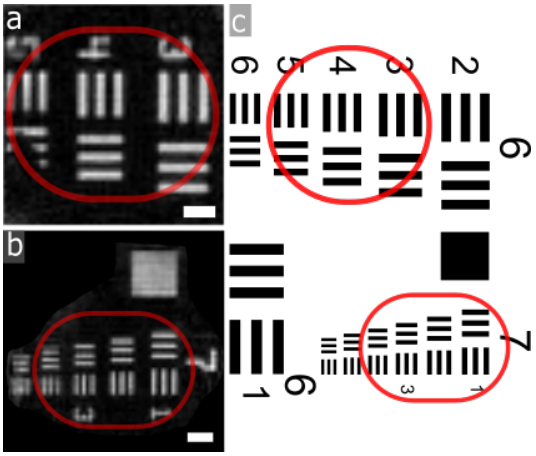

(a) Polarization-split reconstruction

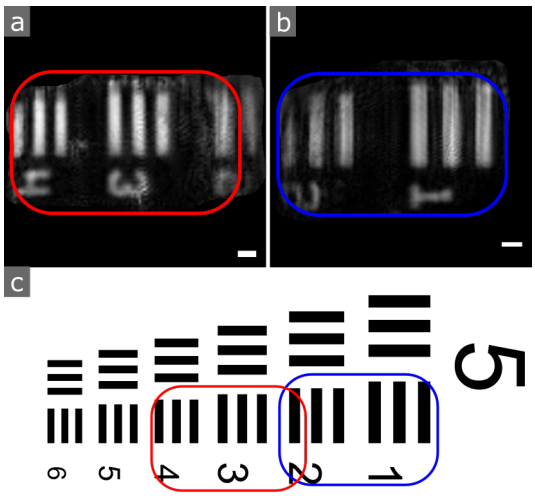

(b) Spectrally-split reconstruction

Figure 43: Reconstruction results from the beam separation ptychography experiments. Subfigure 43a compares the reconstructions of the object amplitudes for both the parallel and normal polarizations with the microscope image of the sample. Each separated probe scanned a unique region and recovered an image of the scanned area. Similarly Figure 43b compares results from the spectrally separated beams compared with the microscope image. Scale bars are all $20\mu m$.

We have shown that multiple areas of a sample can be imaged simultaneously by spatially separating probes for a ptychography scan. The spatial resolution of all recovered images match the expected resolution limits for their respective wavelengths. Spatially separating multiplexed scanning has application in HHG sources since the harmonics in the Dirac comb distribution may be spatially separated with only a few additional optical components.

5.6 Conclusion

Ultimately the ptychography prototype is a huge success both in terms of resolving small objects and in terms of allowing for rapid development of ptychographic imaging techniques. Here I showed how to assemble a ptychography microscope and demonstrated that it is possible to implement hyper-spectral ptychography with a broad bandwidth illumination. Furthermore as a group we explored mutual incoherence ptychography by separating the probe both spectrally and by polarization.

In constructing this ptychography prototype I learned a tremendous amount of knowledge and gained incredible experience. I built and aligned the base ptychography experiment, and aligned subsequent ptychography experiments (except for the spectral and polarization split experiments where I still contributed to the experimental design). I wrote three helpful simulations for testing various conceptual aspects of the experiment. I worked with PI stages and a Mightex camera to collect data. I wrote dynamic ranging code for the data collection process. The rendered images are my own developed 3D models. Additionally all reconstructions are my own work, though I use the group's ePIE reconstruction algorithm. The experience I received during this project was incredible and I am grateful to have work on such engaging research.

These successes are very promising for application in the EUV and soft X-ray regime. What is even more exciting is the future work that can be done and the future ideas that can be explored using the optical prototype. With this prototype we can attempt reconstructions with color-responsive samples to show the power of ptychography in distinguishing images via chemical specificity. We can also rearrange the end of the optical track for reflection geometry so that the collected light from the sample is from its reflection rather than its transmission. This has the added benefit of allowing us to collect topographic information of the sample and overcome the 2π phase ambiguity tied with single-color ptychography. We can even attempt time-dynamical imaging using the broad-bandwidth source on the ptychography prototype. There are no limits to how this prototype may be configured or modified to pioneer the world of coherent diffractive imaging. I am excited to see where the experiment goes next.

Acknowledgements

I would like to acknowledge my principle investigators Henry Kapteyn, Margaret Murnane, and Daniel Adams, my post doctoral researcher Giulia Mancini, my primary mentor Dennis Gardner, and my other mentors Charlie Bevis, Robert Karl, Elisabeth Shanblatt, Michael Tanksalvala, and Christina Porter. They have all made my experience in research fulfilling and have pushed my boundaries of understanding. Thank you all.

References

[1] J R Fienup. Reconstruction of an object from the modulus of its Fourier transform. *Optics letters*, 3(1):27–29, 1978.

[2] Jianwei Miao, Pambos Charalambous, Janos Kirz, and David Sayre. Extending the methodology of X-ray crystallography to allow imaging of micrometre-sized non-crystalline specimens. *Nature*, 400(6742):342–344, 1999.

[3] I K Robinson, J L Libbert, I a Vartanyants, J a Pitney, D M Smilgies, D L Abernathy, and G Grübel. Coherent x-ray diffraction imaging of silicon oxide growth. *Physical Review B*, 60(14):9965–9972, 1999.

[4] S. Marchesini, H. He, H. N. Chapman, S. P. Hau-Riege, A. Noy, M. R. Howells, U. Weierstall, and J. C. H. Spence. X-ray image reconstruction from a diffraction pattern alone. *Physical Review B*, page 5, 2003.

[5] Darren J. Batey, Daniel Claus, and John M. Rodenburg. Information multiplexing in ptychography. *Ultramicroscopy*, 138:13–21, 2014.

[6] Andrew M. Maiden and John M. Rodenburg. An improved ptychographical phase retrieval algorithm for diffractive imaging. *Ultramicroscopy*, 109(10):1256–1262, 2009.

[7] A.G Fallis. Theory of high-harmonic generation by low-frequency laser fields. *Journal of Chemical Information and Modeling*, 53(9):1689–1699, 2013.

[8] Pierre Thibault. High-Resolution Scanning X-ray. *Science*, 379(2008):379–383, 2009.

[9] J W Goodman. *Introduction to Fourier Optics*. Roberts and Company, 2005.

[10] J. M. Rodenburg. Ptychography and related diffractive imaging methods. *Advances in Imaging and Electron Physics*, 150(07):87–184, 2008.

[11] T. B. Edo, D. J. Batey, A. M. Maiden, C. Rau, U. Wagner, Z. D. Pe, T. A. Waigh, and J. M. Rodenburg. Sampling in x-ray ptychography. *Physical Review A - Atomic, Molecular, and Optical Physics*, 87(5):1–8, 2013.

[12] R.W. Gerchberg. Super-resolution through Error Energy Reduction. *Optica Acta: International Journal of Optics*, 21(9):709–720, 1974.

[13] J R Fienup. Phase retrieval algorithms: a comparison. *Applied optics*, 21(15):2758–2769, 1982.

[14] Andrew M. Maiden and John M. Rodenburg. An improved ptychographical phase retrieval algorithm for diffractive imaging. *Ultramicroscopy*, 109(10):1256–1262, 2009.

[15] Daniel W.E. Noom, Dirk E. Boonzajer Flaes, Elias Labordus, Kjeld S.E. Eikema, and Stefan Witte. High-speed multi-wavelength Fresnel diffraction imaging. *Optics Express*, 22(25):30504–11, 2014.

[16] Pierre Thibault and Ivan C. Rankenburg. Optical diffraction microscopy in a teaching laboratory. *American Journal of Physics*, 75:827, 2007.

[17] Robert Karl, Charles Bevis, Raymond LopezRios, Jonathan Reichanadter, and Dennis Gardner. Spatial, Spectral, and Polarization Multiplexed Ptychography. *Arxiv preprint arXiv:1401.4101*, 72:12, 2014.

[18] Pierre Thibault and Andreas Menzel. Reconstructing state mixtures from diffraction measurements supplement. *Nature*, 494(7435):68–71, 2013.

[19] B. Enders, M. Dierolf, P. Cloetens, M. Stockmar, F. Pfeiffer, and P. Thibault. Ptychography with broad-bandwidth radiation. *Applied Physics Letters*, 104(17), 2014.

[20] Ivan Christov, Margaret Murnane, and Henry Kapteyn. High-Harmonic Generation of Attosecond Pulses in the Single-Cycle Regime. *Physical Review Letters*, 78(7):1251–1254, 1997.

[21] J. Zhou, J. Peatross, M. Murnane, H. Kapteyn, and I. Christov. Enhanced High-Harmonic Generation Using 25 fs Laser Pulses. *Physical Review Letters*, 76(5):752–755, 1996.

[22] Zenghu Chang, Andy Rundquist, Haiwen Wang, Margaret Murnane, and Henry Kapteyn. Generation of Coherent Soft X Rays at 2.7 nm Using High Harmonics. *Physical Review Letters*, 79(16):2967–2970, 1997.

[23] a. Rundquist. Phase-Matched Generation of Coherent Soft X-rays. *Science*, 280(5368):1412–1415, 1998.

[24] M. C. Chen, P. Arpin, T. Popmintchev, M. Gerrity, B. Zhang, M. Seaberg, D. Popmintchev, M. M. Murnane, and H. C. Kapteyn. Bright, coherent, ultrafast soft x-ray harmonics spanning the water window from a tabletop light source. *Physical Review Letters*, 105(17):1–4, 2010.

[25] T. Popmintchev, M.-C. Chen, D. Popmintchev, P. Arpin, S. Brown, S. Alisauskas, G. Andriukaitis, T. Balciunas, O. D. Mucke, a. Pugzlys, a. Baltuska, B. Shim, S. E. Schrauth, a. Gaeta, C. Hernandez-Garcia, L. Plaja, a. Becker, a. Jaron-Becker, M. M. Murnane, and H. C. Kapteyn. Bright Coherent Ultrahigh Harmonics in the keV X-ray Regime from Mid-Infrared Femtosecond Lasers. *Science*, 336(6086):1287–1291, 2012.